

## Error scaling of large-eddy simulation in the outer region of wall-bounded turbulence

Adrián Lozano-Durán<sup>a,\*</sup>, Hyunji Jane Bae<sup>b</sup>

<sup>a</sup>Center for Turbulence Research, Stanford University, Stanford, California 94305, USA

<sup>b</sup>Graduate Aerospace Laboratories, California Institute of Technology, Pasadena, California, 91125

### ARTICLE INFO

#### Article history:

Received 1 May 2018

Received in final form 10 May 2018

Accepted 13 May 2018

Available online 15 May 2018

### ABSTRACT

We study the error scaling properties of large-eddy simulation (LES) in the outer region of wall-bounded turbulence at moderately high Reynolds numbers. In order to avoid the additional complexity of wall-modeling, we perform LES of turbulent channel flows in which the no-slip condition at the wall is replaced by a Neumann condition supplying the exact mean wall-stress. The statistics investigated are the mean velocity profile, turbulence intensities, and kinetic energy spectra. The errors follow  $(\Delta/L)^\alpha Re_\tau^\gamma$ , where  $\Delta$  is the characteristic grid resolution,  $Re_\tau$  is the friction Reynolds number, and  $L$  is the meaningful length-scale to normalize  $\Delta$  in order to collapse the errors across the wall-normal distance. We show that  $\Delta$  can be expressed as the  $L_2$ -norm of the grid vector and that  $L$  is well represented by the ratio of the friction velocity and mean shear. The exponent  $\alpha$  is estimated from theoretical arguments for each statistical quantity of interest and shown to roughly match the values computed by numerical simulations. For the mean profile and kinetic energy spectra,  $\alpha \approx 1$ , whereas the turbulence intensities converge at a slower rate  $\alpha < 1$ . The exponent  $\gamma$  is approximately 0, i.e. the LES solution is independent of the Reynolds number. The expected behavior of the turbulence intensities at high Reynolds numbers is also derived and shown to agree with the classic log-layer profiles for grid resolutions lying within the inertial range. Further examination of the LES turbulence intensities and spectra reveals that both quantities resemble their filtered counterparts from direct numerical simulation (DNS) data, but that the mechanism responsible for this similarity is related to the balance between the input power and dissipation rather than to filtering.

© 2019 Elsevier Inc. All rights reserved.

\*Corresponding author: Tel.: +0-000-000-0000; fax: +0-000-000-0000;  
e-mail: [adrianld@stanford.edu](mailto:adrianld@stanford.edu) (Adrián Lozano-Durán)

## 1. Introduction

Most turbulent flows cannot be calculated by DNS of the Navier-Stokes equations because the range of scales of motions is so large that the computational cost becomes prohibitive. In LES, only the large eddies are resolved, and the effect of the small scales on the larger scales is modeled through an SGS model. The approach enables a reduction of the computational cost by several orders of magnitude while still capturing the statistical quantities of interest. However, the solutions provided by most LES approaches are grid-dependent, and multiple computations are required in order to faithfully assess the quality of the LES results. This brings the fundamental question of what is the expected LES error as a function of Reynolds number and grid resolution. The necessity of assessing the impact of grid resolution on both the accuracy and convergence properties of SGS models and flow statistics has been highlighted in the NASA Vision 2030 [1] as a pacing item for computational fluid mechanics. The issue was also remarked by Pope [2] as a central problem concerning the foundations of LES. Therefore, LES should not be framed as the result of one single solution, but instead as a convergence study using multiple grid resolutions. It is then pertinent to determine the grid requirements in order to deem LES as a cost-saving approach compared to DNS. In the present work, we analyze the LES error scaling of the mean velocity profile, turbulence intensities, and energy spectra in the outer region of wall-bounded flows without the influence of the wall.

The equations for LES are formally derived by applying a low-pass filter to the Navier–Stokes equations [3]. The common procedure is then to solve these filtered equations together with a model for the SGS stresses, but no explicit filter form is usually specified. Instead, the discrete differentiation operators and limited grid resolution used to compute the LES solution are assumed to act as an effective implicit filter [4, 5, 6, 7]. The approach, usually referred to as implicitly-filtered LES, yields a velocity field that is considered representative of the actual filtered velocity with filter size proportional to the grid resolution [4, 8]. This lack of explicit filtering is responsible for the aforementioned intimate relation between the grid resolution and the LES equations [9]. Grid convergence is only guaranteed in the limit of DNS-like resolution, and the LES predictions may be sensitive in an intricate manner to the grid size above such a limit. This is a distinctive feature of implicitly-filtered LES which entails important difficulties for evaluating the quality of the solutions.

First studies aiming to assess the accuracy of SGS models include the pioneering investigation by Clark et al. [10], who established the numerical study of decaying isotropic turbulence as a reference benchmark, although the grid resolutions and Reynolds numbers tested were highly constrained by the computational resources of the time. Since then, common benchmarks for LES have broadened to include simple hydrodynamic cases such as forced or decaying isotropic turbulence [11], rotating homogeneous turbulence [12], spatial or temporal mixing layers [13, 14] and plane turbulent channel flow [15, 16, 17], among others. See [18] for an overview of cases for LES validation.

The analysis of discretization errors in LES by Ghosal [19], Kravchenko and Moin [20] and Chow and Moin [21] revealed that the magnitude of the numerical errors can be comparable to those from SGS modeling. Recent developments in modeling and numerical error quantification in isotropic turbulence by Meyers et al. [22] also showed that the partial cancellation of both sources can lead to coincidentally accurate results. Along the same line, Meyers et al. [23] studied the combined effect of discretization and model errors, and a further series of works resulted in the error-landscape-methodology framework reviewed by Meyers [24], where it is stressed that the determination of the quality of LES based on one single metric alone may produce misleading results. The performance of SGS models in the presence of walls is even more erratic. Meyers and Sagaut [25] investigated the grid convergence behavior of channel flow DNS at resolutions typically encountered in SGS model testing. They observed a non-monotonic convergence of the skin friction and turbulence intensities with grid-refinements, suggesting that the robustness of SGS models should be tested for a range of Reynolds numbers and resolutions in order to avoid incidental coincidences with DNS results. At much higher Reynolds numbers, Sullivan and Patton [26] examined the numerical convergence of LES in time-dependent weakly sheared planetary boundary layers. They assessed the convergence of the second-order statistics, energy spectra, and entertainment statistics, and concluded that LES solutions are grid-independent provided that there is adequate separation between the energy-containing eddies and those near the filter cut-off scale. Stevens et al. [27] showed the ability of LES to reproduce accurately second and higher-order velocity moments for grid resolutions fine enough to resolve 99% of the LES kinetic energy. The convergence of SGS models in complex geometries has been explored in a lesser degree, but some noteworthy efforts are the pulsatile impinging jet in turbulent cross-flow by Toda et al. [28] and the full plane calculations using the NASA Common Research Model by Lehmkühl et al. [29].

A central matter among the convergence studies above is the search for the most meaningful flow quantity to collapse the LES errors when the grid size, Reynolds number, and model parameters are systematically varied. Geurts

and Fröhlich [30] characterized the simulation errors in terms of the subgrid-activity, defined as the the relative subgrid-model dissipation rate with respect to the total dissipation rate. Klein [31] studied the accuracy of single-grid estimators for the unresolved turbulent kinetic energy to assess the quality of LES, and evaluated the sensitivity of the LES results on the modeling and numerical errors. Similarly, Freitag and Klein [32] presented a method to evaluate error contributions by assuming that the numerical and modeling errors scale as a power of the grid spacing and filter width, respectively. Other indices to estimate the quality of the LES solution are the fraction of the total turbulent kinetic energy in the resolved motions [2], the relative grid size with respect to Kolmogorov or Taylor scales, or the effective eddy viscosity compared to the molecular viscosity [33]. Alternative and more sophisticated metrics are still emerging, for instance, the Lyapunov exponent measurement proposed by Nastac et al. [34] for assessing the dynamic content and predictability of LES among others, but there is a lack of consensus regarding which should be the most meaningful metric to quantify errors in a general set-up, if any.

In the present work, we study the error scaling of SGS models based on the eddy viscosity assumption in the outer region of wall-bounded turbulence at moderately high Reynolds numbers. Our goal is to characterize the errors as a function of grid resolution and Reynolds number, and to find the physical length-scale dictating the relative size of the grid that is relevant for error quantification. For that purpose, we perform a theoretical estimation of the error scaling for the mean velocity profile, turbulence intensities, and kinetic energy spectra. Our results are numerically corroborated by LES of turbulent channel flows using a wall model that acts as a surrogate of the near-wall dynamics by supplying the exact mean wall-stress. This numerical set-up is motivated by previous DNS and LES studies showing that the features of the outer flow are reproduced with reasonably good fidelity even if the near-wall layer is poorly represented [35, 36, 37, 38, 39]. Finally, it is important to remark that turbulent free shear flows such as mixing layers, jets, and wakes are also tenable candidates for studying shear-dominated flows away from walls. However, their large scales are dynamically different to the large scale motions of turbulent boundary layer flows typically relevant for external aerodynamics, which is the focus of the present study.

The manuscript is organized as follows. In Section 2, we illustrate the challenge of assessing the performance of SGS models in the outer layer of wall-bounded turbulence. We discuss the methodology and numerical setup to assess the convergence of SGS models in Section 3. The results for the errors in the mean velocity profile are presented in Section 4, for the turbulence intensities in Section 5, and for the energy spectra in Section 6. Finally, we conclude in Section 7.

## 2. The challenge of quantifying the performance of SGS models in the outer region of wall turbulence

Most SGS models assume that a considerable fraction of the turbulent kinetic energy (i.e., 80-90% [2]) is resolved by the grid, and the Reynolds numbers and grid resolutions must comply with this requirement in order to faithfully assess the performance of the models. In unbounded flows, such as isotropic turbulence, LES can be performed at relatively coarse grid resolutions while still meeting this condition. On the contrary, the scenario is not as favorable for wall-bounded flows as discussed below. The number of grid points  $N$  to compute a turbulent boundary layer of thickness  $\delta$  spanning a wall-parallel area of  $L_1 \times L_3$  is

$$N = \int_0^{L_1} \int_0^\delta \int_0^{L_3} \frac{dx_1 dx_2 dx_3}{\Delta_1 \Delta_2 \Delta_3}, \quad (1)$$

where  $x_1$ ,  $x_2$  and  $x_3$  are the streamwise, wall-normal, and spanwise directions, respectively, and  $\Delta_1$ ,  $\Delta_2$ , and  $\Delta_3$  are the target grid resolutions in each direction which in general are a function of space. The required number of grid points can be expressed as  $N \sim Re^\zeta$ , where the exponent  $\zeta$  depends on the sizes of the eddies expected to be accurately represented by the grid. Estimations of  $\zeta$  can be found in Chapman [40] and Choi and Moin [41]. DNS aims to capture eddies in the dissipative range, and hence  $\Delta_i \sim \eta$  and  $\zeta \approx 2.6$ , where  $\eta$  is the Kolmogorov length-scale. To resolve the energy-containing eddies as in traditional LES (also referred to as wall-resolved LES or WRLES),  $\Delta_i$  should scale as the integral length scale,  $\Delta_i \sim L_\varepsilon$ , which yields  $\zeta \approx 1.9$ . In the logarithmic region (log layer) of wall-bounded flows,  $L_\varepsilon$  grows linearly with  $x_2$  and the energy-containing eddies have sizes proportional to the distance to the wall [42, 43]. Consequently, the LES grid must be accordingly reduced in all the spatial directions to resolve a constant fraction of the turbulent kinetic energy, increasing the computational cost. WRLES can be properly performed through nested grids [44, 45] such as the one depicted in Fig. 1. Otherwise, the near-wall grid resolution does not suffice to capture the energy-containing eddies, and most SGS models perform poorly [46]. Finally, if we target to model only the outer

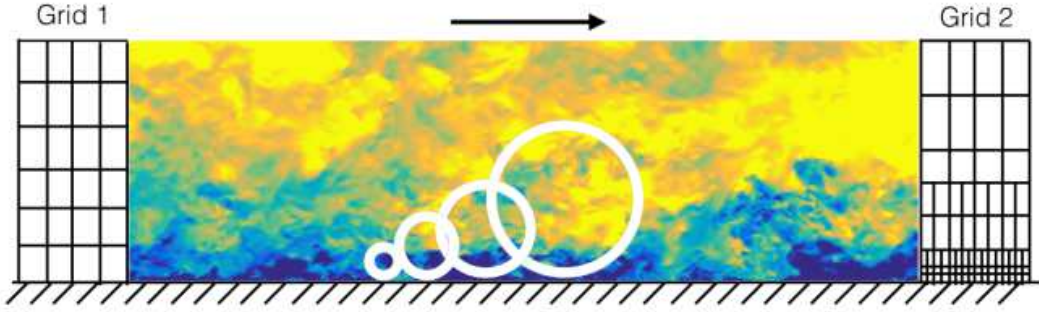


Fig. 1: Instantaneous streamwise velocity in a turbulent channel flow at  $Re_\tau \approx 4200$  and sketch of wall-attached eddies of different sizes (white circles). Colors range from blue (low velocity) to yellow (high velocity). Grid 1 (left) depicts a uniform grid typical of WMLES. Grid 2 (right) represents a nested grid necessary for proper WRLES.

flow motions as in wall-modeled LES (WMLES), the grid requirements are such that  $\Delta_i \sim \delta$ , and  $\zeta \leq 1$  depending on the wall model approach.

Although WRLES has been practiced for a long time, actual WRLES is scarce due to the complexity of its implementation and its associated computational cost. In typical WRLES studies, only the wall-normal resolution is properly refined according to the size of the energy-containing eddies, while the wall-parallel directions remain under-resolved. Most of the grid convergence studies in wall-bounded LES mentioned in the introduction fall within this category. The consequence is that the majority of previous validation works are performed at relatively low Reynolds numbers to make the calculations computationally affordable [41] and to avoid the errors of under-resolving the wall-parallel directions. Under these conditions, it is questionable whether SGS models are active enough to adequately measure their performance in the outer layer of wall turbulence.

To illustrate the low contribution of SGS models far from the wall and their poor performance in the near-wall region, Fig. 2 shows the mean streamwise velocity profile,  $\langle \tilde{u}_1 \rangle$ , for an LES turbulent channel flow as a function of the wall-normal distance. The details of the simulations are discussed in Section 3.2 (see Table 1), but for now, it is only important to remark that all cases were computed using identical grids (with 13 points per boundary layer thickness) and friction Reynolds number,  $Re_\tau \approx 950$ . Coarse DNS (no SGS model and no wall model) provides the worst prediction (squares in Fig. 2). Ideally, a perfect SGS model would supply the missing stresses at all distances from the wall. Indeed, Fig. 2 shows that the solution improves by introducing the dynamic Smagorinsky model (circles); however, the performance is still poor and  $\langle \tilde{u}_1 \rangle$  is far from the reference DNS velocity profile. In contrast, the agreement with DNS in the outer layer ( $x_2 \gtrsim 0.2\delta$ ) is excellent when the equilibrium wall model from Kawai and Larsson [47] is employed (triangles), despite the fact that there is no explicit SGS model in this case.

Note that for all cases, the shape of  $\langle \tilde{u}_1 \rangle$  far from the wall is close to the DNS solution and barely affected by the presence or lack thereof of an SGS model. The main source of error comes from the inaccurate prediction of the wall friction velocity,  $u_\tau$ , which translates into the overprediction of  $\langle \tilde{u}_1^+ \rangle = \langle \tilde{u}_1 \rangle / u_\tau$ . This suggests that the application of traditional SGS models alone is not sufficient to provide the correct stress at the wall, problem that is attenuated by means of a wall model. The result highlights the importance of wall-modeling, but also shows that the validation of SGS models in the outer layer of wall turbulence at low Reynolds numbers or very fine grid resolutions could be meaningless due to the low activity of the models themselves in this regime. On the contrary, accurate quantification of SGS model errors could be achieved by performing true WRLES using three-dimensional grid refinement as Grid 2 in Fig. 1. However, we have mentioned above that the latter is not a common practice, and most attempts at WRLES suffer from the limitation demonstrated in Fig. 2. Therefore, many of the mismatches in the mean velocity profile between DNS and LES reported in the literature are probably dominated by errors accumulated near the wall. This calls for new numerical benchmarks aiming to isolate LES errors in the outer flow from the region closest to the wall. In the present work we propose a new benchmark to overcome this limitation.

The behavior of SGS models close to the wall has been improved in recent works such as the constrained LES by Chen et al. [48], the integral length-scale approximation model by Rouhi et al. [49], and the explicit algebraic

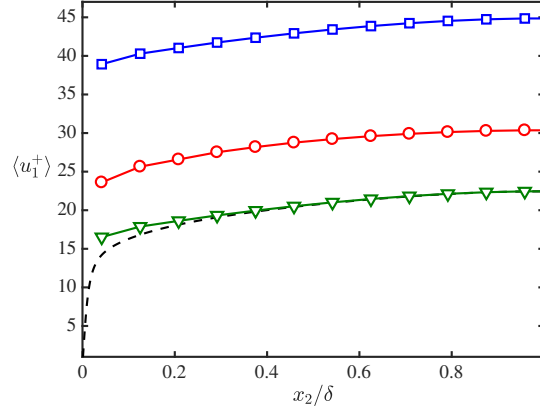


Fig. 2: Mean streamwise velocity profile,  $\langle u_1^+ \rangle$ , for a turbulent channel flow as a function of the wall-normal distance,  $x_2$ , scaled by the channel half-height,  $\delta$ . Lines and symbols are: ( $\square$ ), no explicit SGS model with no-slip boundary condition at the wall (case NM950-NS); ( $\circ$ ), dynamic Smagorinsky model with no-slip boundary condition at the wall (case DSM950-NS); ( $\nabla$ ), no explicit SGS model with equilibrium wall model from Kawai and Larsson [47] (case NM950-EQWM); ( $\leftarrow$ ), DNS. All cases are at friction Reynolds number  $Re_\tau \approx 950$ . More details are provided in Table 1.

model by Rasam et al. [50], among others. These approaches reduce substantially the grid requirements by modifying the SGS model near the wall while maintaining the no-slip boundary condition. Nevertheless, in the present work we focus on the error analysis within the outer flow far from the wall, and the aforementioned SGS models are not considered.

### 3. Benchmark for the outer region of wall-bounded turbulence

#### 3.1. Exact mean wall-stress turbulent channel flows

We consider a plane turbulent channel flow with periodic boundary conditions in the streamwise and spanwise directions. The incompressible LES equations are obtained by applying a spatial filter to the Navier–Stokes equations,

$$\frac{\partial \bar{u}_i}{\partial t} + \frac{\partial \bar{u}_i \bar{u}_j}{\partial x_j} + \frac{\partial \tau_{ij}}{\partial x_j} = -\frac{1}{\rho} \frac{\partial \bar{p}}{\partial x_i} + \nu \frac{\partial^2 \bar{u}_i}{\partial x_j \partial x_j}, \quad \frac{\partial \bar{u}_i}{\partial x_i} = 0, \quad (2)$$

where  $\bar{u}_i$  for  $i = 1, 2, 3$  are the streamwise, wall-normal and spanwise filtered velocities, respectively,  $\bar{p}$  is the filtered pressure,  $\tau_{ij} = \overline{u_i u_j} - \bar{u}_i \bar{u}_j$  is the effect of the sub-filter scales on the resolved eddies,  $\rho$  is the flow density, and  $\nu$  is the kinematic viscosity. The streamwise, wall-normal and spanwise spatial directions are  $x_i$  for  $i = 1, 2, 3$ , respectively, and the walls are located at  $x_2 = 0\delta$  and  $x_2 = 2\delta$ . The objective of LES modeling is to approximate  $\tau_{ij}$  via the SGS tensor  $\tau_{ij}^{\text{SGS}}$ . To emphasize that an LES model is not exact, the resolved LES velocity is denoted by  $\tilde{u}_i$  and we expect that  $\tilde{u}_i \approx \bar{u}_i$  for an accurate SGS model.

We have discussed in Section 2 the necessity of benchmarks for wall-bounded turbulence that are independent of the strict near-wall resolution requirements. To attain this goal, the no-slip boundary condition at the wall is replaced by a constant wall-stress condition imposed through a Neumann boundary condition of the form

$$\frac{\partial \tilde{u}_i}{\partial n} \Big|_w = \frac{\tau_w - \tau_{12}^{\text{SGS}} \Big|_w}{\nu}, \quad (3)$$

where  $w$  denotes quantities evaluated at the wall,  $n$  is the wall-normal direction oriented towards the interior of the channel, and  $\tau_w$  is the mean wall stress known *a priori* from DNS. Equation (3) can be thought of as a wall-model supplying the exact mean wall stress. Equation (3) is used here in the context of LES, but a similar shear-stress boundary condition was used by Chung et al. [39] to study Townsend’s outer-layer similarity hypothesis in DNS.

The set-up above is not intended to capture the near-wall dynamics, and the small eddies close to the wall are prone to be misrepresented when Eq. (2) is discretized for coarse grid resolutions. However, our focus is on the outer

Case	SGS model	Wall condition	$Re_\tau$	$\Delta_1/\delta$	$\Delta_2/\delta$	$\Delta_3/\delta$
NM950-NS	NM	NS				
DSM950-NS	DSM	NS	932	0.10	0.080	0.050
NM950-EQWM	NM	EQWM				

Table 1: List of cases used in Section 2. The second column contains the SGS model: no explicit SGS model (NM) or dynamic Smagorinsky model (DSM). The third column refers to the wall boundary condition: no-slip (NS) or Neumann boundary condition using the equilibrium wall-model from Kawai and Larsson [47] (EQWM). The fourth column indicates the friction Reynolds number.  $\Delta_1$ ,  $\Delta_2$ , and  $\Delta_3$  are the streamwise, wall-normal, and spanwise grid resolutions respectively.

flow along the range  $0.2\delta < x_2 < \delta$  [51], and previous studies have revealed that the flow statistics and structure of this region are relatively independently of the particular configuration of the eddies closest to the wall, even if they are partially or completely under-resolved. Some examples are the roughness experiments in channels and boundary layers [52, 53, 54, 36, 55], and the idealized numerical studies by Flores and Jiménez [36], Mizuno and Jiménez [38], Chung et al. [39] and Lozano-Durán and Bae [56], among others. In all these cases, the near-wall region was seriously modified or directly bypassed, but the properties of the outer layer remained essentially unaltered. This is also the case for WMLES, where it has been shown that imposing the correct mean wall-stress is sufficient to predict one-point statistics accurately [37], consistent with the approach in Eq. (3). Therefore, the correct representation of the outer layer dynamics remains uncoupled from the inner layer structure, supporting the numerical experiment presented here as a valid framework to assess LES errors far from the wall. The independence of the outer flow with respect to the near-wall dynamics together with the existence of inner-outer scale separation are the main assumptions of the current numerical set-up. Nonetheless, it has been reported in previous works that some flow configurations, such as boundary layers subjected to strong spanwise wall-stress variations [57], may invalidate these assumptions.

### 3.2. Numerical experiments

We perform a set of LES of plane turbulent channels driven by a constant mass flow in the streamwise direction. The simulations are computed with a staggered, second-order, finite difference [58] and fractional-step method [59] with a third-order Runge-Kutta time-advancing scheme [60]. The code has been validated in previous studies in turbulent channel flows [61, 62] and flat-plate boundary layers [63]. Periodic boundary conditions are imposed in the streamwise and spanwise directions, while for the top and bottom walls we use either the no-slip (NS) boundary condition or exact-wall-stress (EWS) Neumann boundary condition from Eq. (3).

Two SGS models are investigated: dynamic Smagorinsky model (DSM) [16, 64] and anisotropic minimum dissipation (AMD) model [65], which are regarded as representative eddy-viscosity models with and without test filtering, respectively. We also consider cases without an explicit SGS model (NM) where the numerical truncation errors act as an implicit SGS model. Some of our results have also been computed for the Vreman model [66] (see Appendix A) whose performance was found to be similar to AMD.

The size of the computational domain is  $8\pi\delta \times 2\delta \times 3\pi\delta$  in the streamwise, wall-normal, and spanwise directions, respectively. The grid resolutions are denoted by  $\Delta_1$ ,  $\Delta_2$ , and  $\Delta_3$  for each spatial direction, and they range from  $0.025\delta$  to  $0.2\delta$ , which correspond to 5 to 40 points per boundary layer thickness. The present grids are in accordance with the typical grid resolutions encountered in WMLES of real external aerodynamic applications, and follow the recommendations by Chapman [40] for resolving the large eddies in the outer region of wall turbulence. Four different friction Reynolds numbers are considered,  $Re_\tau = u_\tau\delta/\nu \approx 950, 2000, 4200$  and  $8000$ , where  $u_\tau$  is the friction velocity at the wall. The LES results are compared with reference DNS data from Hoyas and Jiménez [67], Lozano-Durán and Jiménez [68], and Yamamoto and Tsuji [69]. All the LES channel flow were run at least for  $100\delta/u_\tau$  after transients.

The list of cases used in Section 2 is given in Table 1. The simulations discussed for the remainder of the paper are named following the convention [SGS model][ $Re_\tau$ ]-[boundary condition]-[grid resolution], where the grid resolutions are denoted by i1, i2, i3 and i4 for isotropic grids, and by a1, a2 and a3 for anisotropic grids. The different grid resolutions are provided in Table 2. For example, DSM4200-EWS-i2 is an LES channel flow with DSM at  $Re_\tau \approx 4200$ , EWS boundary condition, and grid resolutions  $\Delta_1 = \Delta_2 = \Delta_3 = 0.1\delta$ .

Grid resolution label	$\Delta_1/\delta$	$\Delta_2/\delta$	$\Delta_3/\delta$
i1	0.20	0.20	0.20
i2	0.10	0.10	0.10
i3	0.050	0.050	0.050
i4	0.025	0.025	0.025
a1	0.20	0.10	0.05
a2	0.10	0.10	0.07
a3	0.20	0.10	0.10

Table 2: Tabulated list of resolutions as a fraction of the channel half-height,  $\delta$ . The first column contains the label used for naming the LES cases computed with different grids.  $\Delta_1$ ,  $\Delta_2$ , and  $\Delta_3$  are the streamwise, wall-normal, and spanwise grid resolutions, respectively.

#### 4. Error scaling of the mean velocity profile

We examine first the mean velocity as it is the figure of merit for most LES studies. We assume that  $\langle u_1 \rangle \approx \langle \tilde{u}_1 \rangle$ , where  $\langle \cdot \rangle$  denotes average in homogeneous directions and time, and the LES mean velocity is directly compared with unfiltered DNS data. The approximation is reasonable for quantities dominated by large-scale contributions, as it is the case for  $\langle u_1 \rangle$ . The error for the mean velocity profile is systematically quantified as the average difference of the LES and DNS solutions in the outer region as

$$\mathcal{E}_m = \left[ \frac{\int_{0.2\delta}^{\delta} (\langle \tilde{u}_1 \rangle - \langle u_1 \rangle)^2 dx_2}{\int_{0.2\delta}^{\delta} \langle u_1 \rangle^2 dx_2} \right]^{1/2}, \quad (4)$$

where  $\langle \tilde{u}_1 \rangle$  is obtained from LES, and  $\langle u_1 \rangle$  is evaluated from DNS data. This choice excludes the nonphysical/under-resolved range  $x_2 < 0.2\delta$  for the LES cases using the exact-wall-stress approach as discussed in Section 3.1. For a channel flow driven by constant mass flux,  $Q$ , and exact mean wall-stress, some reference errors can be obtained from two extreme cases, i.e., a fully turbulent profile defined by the flat velocity  $\langle \tilde{u}_1 \rangle = Q/2\delta$ , and the laminar solution represented by the parabolic function  $\langle \tilde{u}_1 \rangle = 3Q/4\delta(2 - x_2/\delta)x_2/\delta$ , with errors equal to  $\mathcal{E}_{m,turb} \approx 0.06$  and  $\mathcal{E}_{m,lam} \approx 0.26$ , respectively, at  $Re_\tau \approx 4200$ .

In general, the error depends on the grid resolution and Reynolds number,

$$\mathcal{E}_m = \mathcal{E}_m(\Delta_1, \Delta_2, \Delta_3, Re_\tau). \quad (5)$$

If we further assume that  $\mathcal{E}_m \sim \Delta^{\alpha_m} Re_\tau^{\gamma_m}$ , where  $\Delta$  is a (yet to be defined) measure of the grid size, the exponents  $\alpha_m$  and  $\gamma_m$  can be theoretically estimated from the error equation and empirically computed from numerical experiments. Both analysis are performed below. Ultimately, we will conclude that LES is a viable approach for computing the outer flow of wall-bounded flows if the empirical values of the exponents are such that  $\alpha_m > 0$  and  $\gamma_m \approx 0$ .

##### 4.1. Theoretical estimations

We estimate the expected error behavior of  $\mathcal{E}_m$  which serves as a reference for the numerical results in the next section. If we assume that the scaling of the integrand in Eq. (4) with  $\Delta_i$  is roughly the same within  $x_2/\delta \in [0.2, 1]$ ,  $\mathcal{E}_m$  can be approximated by

$$\mathcal{E}_m \sim \langle \tilde{u}_1 \rangle - \langle u_1 \rangle, \quad (6)$$

where the denominator of Eq. (4) is discarded as it is only a normalization factor which does not depend on  $\Delta_i$ . Let us consider the streamwise momentum equation

$$\frac{\partial u_1}{\partial t} = -\frac{\partial u_1 u_j}{\partial x_j} - \frac{\partial p'}{\partial x_1} + \frac{u_\tau^2}{\rho\delta}, \quad (7)$$

where the viscous terms are neglected and the pressure gradient is decomposed into mean and fluctuating contributions  $u_\tau^2/(\rho\delta)$  and  $\partial p'/\partial x_1$ , respectively. In the following, we denote fluctuating quantities by  $(\cdot)'$ . After multiplying Eq. (7)

by  $u_1$  and averaging in the homogeneous directions and time, the resulting equation is

$$-\left\langle u_1 \frac{\partial u_1 u_j}{\partial x_j} \right\rangle - \left\langle u_1' \frac{\partial p'}{\partial x_1} \right\rangle + \frac{u_\tau^2}{\rho \delta} \langle u_1 \rangle = 0. \quad (8)$$

A similar equation can be obtained for the filtered streamwise velocity, and after subtraction and manipulation of both equations we obtain

$$\langle \bar{u}_1' \bar{u}_2' \rangle \frac{\partial \langle \bar{u}_1 \rangle}{\partial x_2} - \langle u_1' u_2' \rangle \frac{\partial \langle u_1 \rangle}{\partial x_2} = \frac{1}{2} \frac{\partial}{\partial x_2} \langle u_1' u_1' u_2' - \bar{u}_1' \bar{u}_1' \bar{u}_2' - 2\tau_{12} \bar{u}_1 \rangle + \left\langle u_1' \frac{\partial p'}{\partial x_1} - \bar{u}_1' \frac{\partial \bar{p}'}{\partial x_1} \right\rangle. \quad (9)$$

For a symmetric filter with well-defined, non-zero, second moment in real space, the terms in right-hand side of (9) can be expressed as [70, 71]

$$\bar{u}_1' \bar{u}_1' \bar{u}_2' - u_1' u_1' u_2' = \frac{\bar{\Delta}_i^2}{2} \left( \bar{u}_1' \bar{u}_1' \frac{\partial^2 \bar{u}_2'}{\partial x_i^2} + 2u_1' u_2' \frac{\partial^2 \bar{u}_1'}{\partial x_i^2} \right) + \mathcal{O}(\bar{\Delta}_1^4 + \bar{\Delta}_2^4 + \bar{\Delta}_3^4), \quad (10)$$

$$\bar{u}_1' \frac{\partial \bar{p}'}{\partial x_1} - u_1' \frac{\partial p'}{\partial x_1} = \frac{\bar{\Delta}_i^2}{2} \left( \bar{u}_1' \frac{\partial^3 \bar{p}'}{\partial x_1 \partial x_i^2} + \frac{\partial \bar{p}'}{\partial x_1} \frac{\partial^2 \bar{u}_1'}{\partial x_i^2} \right) + \mathcal{O}(\bar{\Delta}_1^4 + \bar{\Delta}_2^4 + \bar{\Delta}_3^4), \quad (11)$$

$$\tau_{1j} = \bar{\Delta}_i^2 \frac{\partial \bar{u}_1}{\partial x_i} \frac{\partial \bar{u}_j}{\partial x_i} + \mathcal{O}(\bar{\Delta}_1^4 + \bar{\Delta}_2^4 + \bar{\Delta}_3^4), \quad (12)$$

where repeated indices imply summation, and  $\bar{\Delta}_i$  signifies the filter size in the  $i$ -th direction defined as the square root of the second moment of the filter operator

$$\bar{\Delta}_i^2 = \int_{-\infty}^{\infty} \int_{-\infty}^{\infty} \int_{-\infty}^{\infty} x_i^2 H(x_1, x_2, x_3) dx_1 dx_2 dx_3, \quad (13)$$

with  $H$  the filter kernel. In general,  $\bar{\Delta}_i^2 = \bar{c} \Delta_i^2$ , where  $\bar{c}$  is a coefficient that depends on the particular filter shape, e.g., for a box filter  $\bar{c} = 1/12$ . Eqs. (10), (11), and (12) are valid for filter kernels with Fourier transform of class  $C^\infty$ , which is the case for most filters defined in real space such as the Gaussian filter, tophat filters, and all discrete filters [5].

For the rest of the discussion, we neglect terms of the order of  $\mathcal{O}(\bar{\Delta}_i^4)$  and assume that traditional SGS models are a fourth order approximation to  $\tau_{ij}$ . The simplification is useful for estimating the error scaling independently of any particular SGS model. We further assume that, far from the wall, the wall-normal derivative of  $\bar{u}_1$  in Eq. (12) is well approximated using the fluctuating velocity,  $\partial \bar{u}_1 / \partial x_2 = \partial \langle \bar{u}_1 \rangle / \partial x_2 + \partial \bar{u}_2' / \partial x_2 \approx \partial \bar{u}_1' / \partial x_2$ , since in the log layer the gradients can be estimated as  $\partial \langle \bar{u}_1 \rangle / \partial x_2 \approx u_\tau / (\kappa x_2) \ll u_\tau / \Delta_2 \sim \partial \bar{u}_1' / \partial x_2$ , where  $\kappa$  is the von Kármán constant.

Introducing Eqs. (10), (11), and (12) into (9), invoking the simplifications above, and considering the exact mean wall-stress assumption from Section 3.1, the error in the mean velocity profile at  $x_2 = x_2^o$  can be shown to scale as

$$\mathcal{E}_m \sim \bar{\Delta}_i^2 \left\langle \frac{\bar{u}_1' \bar{u}_1' \partial^2 \bar{u}_2'}{4 \partial x_i^2} + u_1' u_2' \frac{\partial^2 \bar{u}_1'}{\partial x_i^2} + \frac{\partial \bar{u}_1'}{\partial x_i} \frac{\partial \bar{u}_2'}{\partial x_i} u_1' + \int_0^{x_2^o} \left( \frac{\bar{u}_1'}{2} \frac{\partial^3 \bar{p}'}{\partial x_1 \partial x_i^2} + \frac{1}{2} \frac{\partial \bar{p}'}{\partial x_1} \frac{\partial^2 \bar{u}_1'}{\partial x_i^2} - \frac{\partial \bar{u}_1'}{\partial x_i} \frac{\partial \bar{u}_j'}{\partial x_i} \frac{\partial \bar{u}_1'}{\partial x_j} \right) dx_2 \right\rangle. \quad (14)$$

Note that the filter sizes in Eq. (14) are arranged in the form  $\bar{\Delta}_i^2 \sim \Delta_i^2$ , which motivates the use of the  $L_2$ -norm of  $(\Delta_1, \Delta_2, \Delta_3)$  as the characteristic grid-size,  $\Delta \sim \sqrt{\Delta_1^2 + \Delta_2^2 + \Delta_3^2}$ , as long as the error is measured according to Eq. (4). Eq. (14) also shows that  $\Delta_i$  does not provide a full description of the error, and that a complete characterization would involve an effective grid size such as

$$\Delta_{\text{eff}} = \sqrt{d_1 \Delta_1^2 + d_2 \Delta_2^2 + d_3 \Delta_3^2}, \quad (15)$$

where  $d_k$ ,  $k = 1, 2, 3$ , are complicated flow-dependent functions from Eq. (14).

Equation (14) can be further exploited to determine the scaling of  $\mathcal{E}_m$  with  $\Delta$  by assuming  $p' \sim u'^2$  and approximating the dependence of  $\bar{u}_i'$ ,  $\frac{\partial^2 \bar{u}_i'}{\partial x_i \partial x_i}$  and  $\frac{\partial \bar{u}_i'}{\partial x_i}$  on  $\Delta$ . A rough estimation is performed by assuming that the kinetic energy



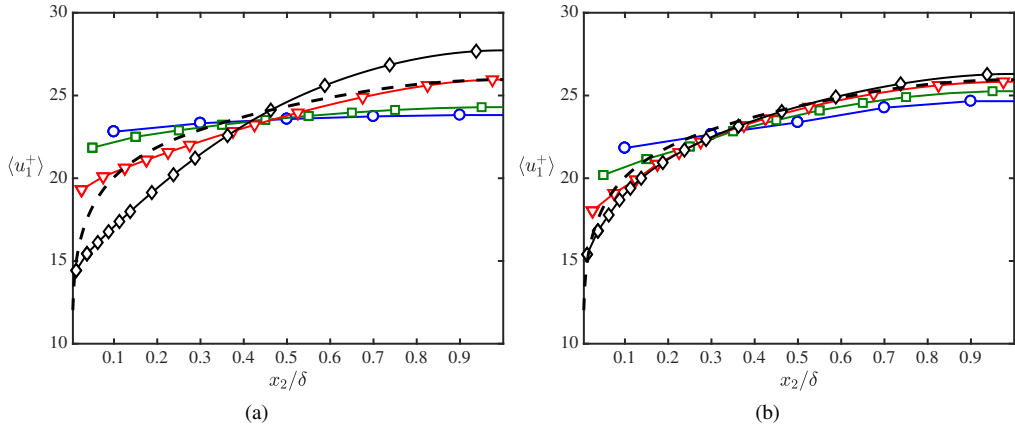


Fig. 3: Mean streamwise velocity profile at  $Re_\tau \approx 4200$  for (a) no explicit SGS model, and (b) DSM. Symbols are for grids i1 ( $\circ$ ), i2 ( $\square$ ), i3 ( $\nabla$ ), and i4 ( $\diamond$ ) from Table 2. The dashed line is DNS.

spectrum follows  $E_K \sim k^\beta$ , with the wavenumber  $k \sim 1/\Delta$ , and the isotropic velocity gradient  $G = \partial u/\partial x$  at scale  $\Delta$  such that

$$\bar{u}'_{1,2} \frac{\partial^2 \bar{u}'_{2,1}}{\partial x_i \partial x_i}, \frac{\partial \bar{u}'_1}{\partial x_i} \frac{\partial \bar{u}'_2}{\partial x_i} \sim G^2 \sim \frac{u^2}{\Delta^2} \sim \frac{k E_K}{\Delta^2} \sim \Delta^{-(\beta+3)}, \quad (16)$$

where the exponent  $\beta$  depends on the regime the SGS models operates: for the shear-dominated range  $\beta = -1$  [52] and  $G^2 \sim \Delta^{-2}$ , whereas for the inertial range  $\beta = -5/3$  [72] and  $G^2 \sim \Delta^{-4/3}$ . Taking into account the scaling above, the expected error in the LES mean velocity profile from Eq. (14) scales as

$$\mathcal{E}_m^s \sim \Delta^0, \quad \mathcal{E}_m^i \sim \Delta, \quad (17)$$

for SGS models acting on the shear-dominated ( $\mathcal{E}_m^s$ ) or inertial ( $\mathcal{E}_m^i$ ) regimes, respectively. The results from Eq. (17) indicate that no improvement in the error is expected for grid resolutions comparable to the scales in the shear-dominated region, whereas an approximately linear improvement can be anticipated for finer grids with sizes comparable to the scales in the inertial range. This suggest that capturing the energy injection mechanism from the mean shear is critical to achieve accurate LES results. The estimations from Eq. (17) assume that  $\Delta$  lies completely either in the inertial range or in the shear-dominated regime. However, the error defined by Eq. (4) accounts for a wide range of wall-normal distances in which  $\Delta$  may change from one regime to the other. In such a case,  $\mathcal{E}_m$  is expected to exhibit an intermediate scaling between  $\mathcal{E}_m^i$  and  $\mathcal{E}_m^s$ . An  $x_2$ -dependent formulation of the error is presented in Section 4.4.

The scaling of  $\mathcal{E}_m$  with  $\Delta$  in Eq. (17) can be estimated from simpler dimensional arguments without going through Eq. (14), but it was beneficial to write the explicit equation of the error to obtain additional information about its functional form. Additionally, it is important to remark that the results from Eq. (17) should be understood as rough estimations since actual errors evolve according to a non-linear equation and, hence, their rigorous mathematical treatment is highly elusive. This consideration is also applicable to the error estimations for the turbulence intensities and energy spectra in later sections.

#### 4.2. Numerical assessment

Fig. 3 shows the mean velocity profiles for a selection of cases at  $Re_\tau \approx 4200$  and different grid resolutions without SGS model (Fig. 3a) and with DSM (Fig. 3b). As expected,  $\langle \tilde{u}_1 \rangle$  converges to  $\langle u_1 \rangle$  as the grid is refined for cases with DSM (equivalently for AMD), while the trend is inconsistent for cases without explicit SGS model.

The quantitative assessment of the  $\mathcal{E}_m$  is shown in Fig. 4(a) as a function of the characteristic grid resolution  $\Delta$ , taken to be

$$\Delta = \sqrt{\frac{\Delta_1^2 + \Delta_2^2 + \Delta_3^2}{3}}, \quad (18)$$

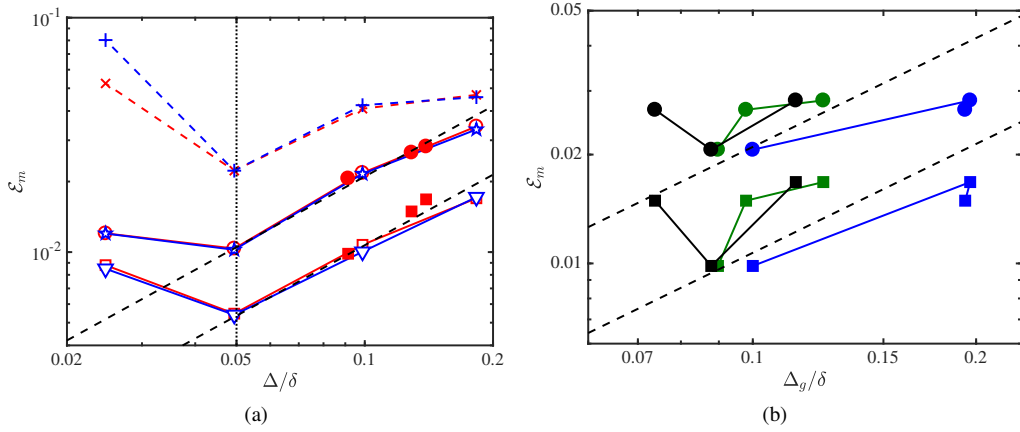


Fig. 4: (a) Error in the mean velocity profile as a function of the characteristic grid resolution  $\Delta = \sqrt{(\Delta_1^2 + \Delta_2^2 + \Delta_3^2)/3}$ . Colors are red, for cases at  $Re_\tau \approx 4200$ , and blue for cases at  $Re_\tau \approx 8000$ . Symbols are (o) and (\*) for DSM, ( $\nabla$ ) and ( $\square$ ) for AMD, ( $\times$ ) and (+) for no explicit SGS model. Open and closed symbols are for isotropic and anisotropic grids, respectively. Dashed lines are  $\mathcal{E}_m = 0.107\Delta/\delta$  and  $\mathcal{E}_m = 0.210\Delta/\delta$ , and the dash-dotted line is  $\Delta/\delta = 0.05$ . (b) Error in the mean velocity profile as a function of alternative characteristic grid sizes:  $\Delta_g = \sqrt[3]{\Delta_1 \Delta_2 \Delta_3}$  (green),  $\Delta_g = \max(\Delta_1, \Delta_2, \Delta_3)$  (blue), and  $\Delta_g = \sqrt{3/(1/\Delta_1^2 + 1/\Delta_2^2 + 1/\Delta_3^2)}$  (black). The results are for cases with anisotropic grids at  $Re_\tau \approx 4200$  with DSM (o), and AMD ( $\square$ ). For reference, panel (b) also includes the dashed lines from panel (a).

as motivated by Eq. (14). Other grid definitions were also inspected such as the cube root of the cell volume [73, 74], the maximum of the grid sizes [75], or the square root of the harmonic mean of the squares of the grid sizes (all reported in Fig. 4b), among others. However, the best collapse is found for the definition in Eq. (18), consistent with the discussion in Section 4.1. A survey of existing subgrid length-scales can be found in Trias et al. [76] but note that in the current study we are discussing the most meaningful grid size to characterize  $\mathcal{E}_m$ , which does not need to coincide with the characteristic length-scale embedded in SGS models (i.e.,  $\tilde{\Delta}$  in the Smagorinsky model  $-2C_s \tilde{\Delta}^2 \sqrt{2\tilde{S}_{nm}\tilde{S}_{nm}}\tilde{S}_{ij}$ , where  $\tilde{S}_{ij}$  is the resolved rate-of-strain tensor and  $C_s$  is a constant).

For cases without SGS model, the errors are discernibly larger than those calculated with DSM or AMD, especially for the finer grid resolutions, and similar to those for fully turbulent flows ( $\mathcal{E}_{m,turb} \approx 0.06$ ). Moreover, they follow a non-monotonic behavior with  $\Delta$ , inconsistent with the second-order prediction from the linear analysis of the spatial discretization errors. This is expected, as the linear analysis holds for  $\Delta \rightarrow 0$ , but it is no longer representative of errors subjected to non-linear diffusion and convection for  $\Delta \sim \delta$ . Visual inspection of the instantaneous streamwise velocity fields for cases without SGS model in Fig. 5 shows that there is a substantial change in the flow topology at  $\Delta \approx 0.05\delta$ . For  $\Delta > 0.05\delta$ , the velocity field lacks the characteristic turbulence features and exhibits instead a highly disorganized structure (Figs. 5a–c). On the other hand, clearly defined streamwise velocity streaks emerge for  $\Delta < 0.05\delta$  (Fig. 5d). We can argue that these streaks are nonphysical in the sense that they worsen the mean velocity profile prediction as shown in Fig. 3(a) for NM4200-EWS-i4.

For cases with SGS model and  $\Delta > 0.05\delta$ , the error follows

$$\mathcal{E}_m \approx \epsilon \left( \frac{\Delta}{\delta} \right) Re_\tau^0, \quad (19)$$

where  $\epsilon$  is a model dependent constant. Note that Eq. (19) is obtained from the numerical evaluation of Eq. (4) using LES data, while Eq. (17) is the scaling analysis of Eq. (4) from theoretical considerations. The results show that the LES solution converges to the correct value free from viscous effects,  $\mathcal{E}_m \sim Re_\tau^0$  (given a perfect wall model for the mean) as demanded by a proper LES far from the walls. Our results also suggest that  $\mathcal{E}_m \sim \Delta$ , which agrees with the theoretical estimation of  $\mathcal{E}_m^i$ , i.e the expected error scaling when  $\Delta$  is of the order of the length-scales in the inertial range. Although both DSM and AMD converge at the same rate with  $\Delta$ , the prefactor  $\epsilon$  can play an important role in the error magnitude and thus different models may be preferred due to their lower  $\epsilon$ . The results in Appendix A show that similar conclusions are drawn for the Vreman model.

For  $\Delta < 0.05\delta$ , the errors depart from  $\mathcal{E}_m \sim \Delta$ . This is probably a complicated non-linear effect which involves the interplay between the numerical scheme and the flow physics. Indeed, the observations from Fig. 5 suggest that there

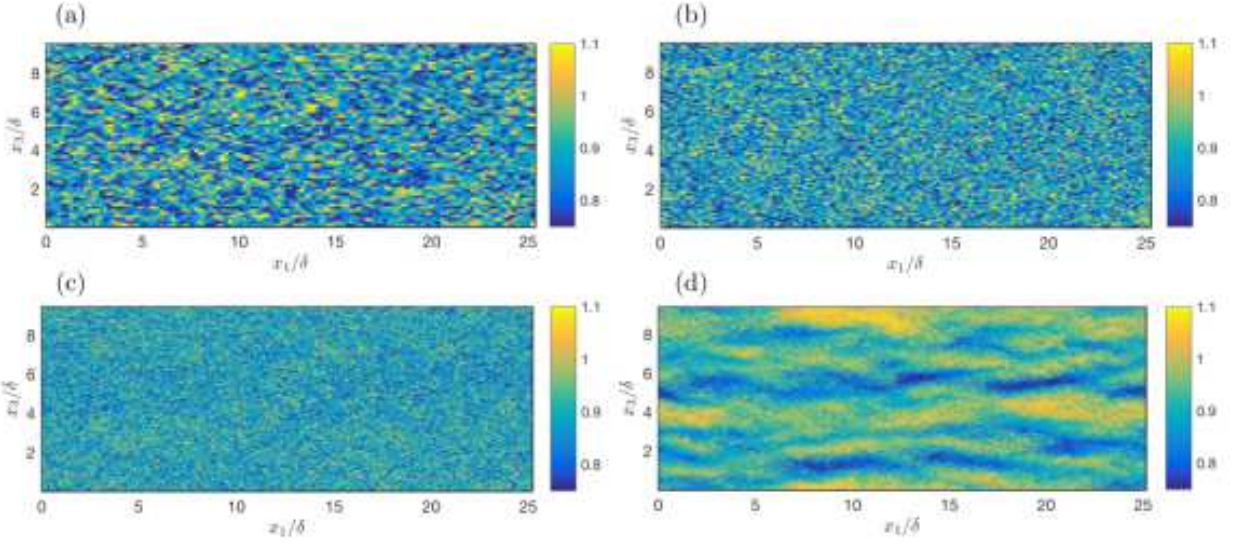


Fig. 5: Instantaneous streamwise velocity in a wall-parallel plane at  $x_2 \approx 0.5\delta$  for (a) NM4200-EWS-i1, (b) NM4200-EWS-i2, (c) NM4200-EWS-i3, (d) NM4200-EWS-i4.

is a competing effect of the improved prediction by the SGS model versus the formation of nonphysical flow structures due to discretization errors. It is shown in Section 6.2 that the grid resolution to resolve 90% of the turbulent kinetic energy is  $\Delta^{\min} \approx 0.04\delta$  at  $x_2 \approx 0.5\delta$  (same as in Fig. 5), that is very close to  $\Delta \approx 0.05\delta$  for which the anomalous behavior of  $\mathcal{E}_m$  appears. This transitional resolution  $\Delta^{\min}$  is related to the ability of the LES solution to support streaks without SGS model, and we can hypothesize that it should have an impact on the behavior of  $\mathcal{E}_m$ , even in the presence of an SGS model. Additional tests included in Appendix A show that the trend  $\mathcal{E}_m \sim \Delta$  is recovered again for finer grids. Although not inspected here, the convergence of  $\langle \tilde{u}_1 \rangle$  towards the DNS solution at even finer grids may entail an intricate non-monotonic response as reported in Meyers and Sagaut [25].

#### 4.3. Alternative metrics for error quantification

Alternative metrics to functionally quantify  $\mathcal{E}_m$  are the resolved total kinetic energy,

$$K_{\text{res}} = \frac{\langle \tilde{u}_i \tilde{u}_i \rangle}{\langle u_i u_i \rangle}, \quad (20)$$

and the SGS activity parameter [30, 22],

$$s = \frac{\langle 2\nu_r \tilde{\mathcal{S}}_{ij} \tilde{\mathcal{S}}_{ij} \rangle}{\langle 2\nu_r \tilde{\mathcal{S}}_{ij} \tilde{\mathcal{S}}_{ij} + 2\nu \tilde{\mathcal{S}}_{ij} \tilde{\mathcal{S}}_{ij} \rangle}, \quad (21)$$

where  $\nu_r$  is the eddy viscosity. The results are shown in Fig. 6 for  $K_{\text{res}}$  and  $s$  averaged over the wall-normal range  $[0.3\delta, \delta]$ . Despite the coarse grid resolutions investigated in the present work, the resolved kinetic energy remains above 90% for all cases (Fig. 6a) and emerges as an effective metric to assess the errors in the mean profile even among different SGS models. The result is not surprising since  $K_{\text{res}}$  can be easily related to  $\mathcal{E}_m$  if we assume that  $\langle u_1^2 \rangle / \langle u_2^2 \rangle \gg 1$  for  $i = 2, 3$ , and  $\langle u_1^2 \rangle \approx \langle u_1 \rangle^2$ . The former are usually  $\sim 100$ , while the last condition is reasonably well satisfied if  $u_1$  follows a normal distribution  $\mathcal{N}(\mu, \sigma)$  with mean  $\mu$  and standard deviation  $\sigma$  such that  $\mu/\sigma \gg 1$ , which is a fair approximation in high-Reynolds-number turbulent channel flows. Under those conditions, the resolved kinetic energy can be expressed as

$$K_{\text{res}} \approx (1 - \mathcal{E}_m)^2, \quad (22)$$

which shows an excellent agreement with the data in Fig. 6(a). Therefore,  $\mathcal{E}_m$  and  $K_{\text{res}}$  are interchangeable metrics for characterizing the errors in  $\langle \tilde{u}_1 \rangle$ . Cases with no explicit SGS model do not follow the trend, and  $K_{\text{res}}$  can even exceed

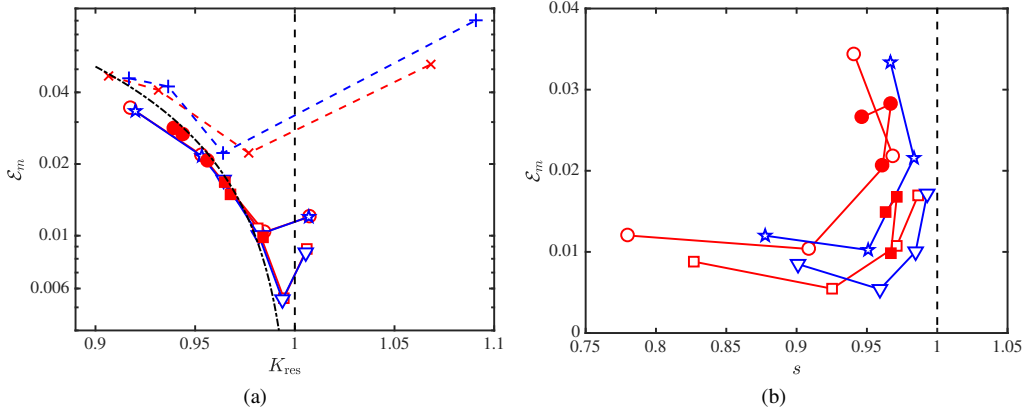


Fig. 6: Error in the mean streamwise velocity profile as a function of (a) the resolved total kinetic energy  $K_{res}$ , and (b) SGS activity parameter  $s$ . Colors are red for cases at  $Re_\tau \approx 4200$ , blue for cases at  $Re_\tau \approx 8000$ . Symbols are (o) and (★) for DSM, (▽) and (□) for AMD, (×) and (+) for no explicit SGS model. Open and closed symbols are for isotropic and anisotropic grids, respectively. The dash-dotted line in (a) is  $K_{res} \approx (1 - \mathcal{E}_m)^2$ . The vertical dashed lines are  $K_{res} = 1$  in (a) and  $s = 1$  in (b).

unity due to nonphysical velocity fluctuations whose origin is discussed in Section 5. The same effect is observed for cases with SGS models for the finest grid resolution but in a lesser degree. The SGS activity is plotted in Fig. 6(b). Increasing  $s$  is associated with increasing  $\mathcal{E}_m$ , although the results are Reynolds number and SGS model dependent and do not collapse for isotropic and anisotropic grids. Equation (21) has still some value as it does not make use of DNS data and it is a more realistic estimator for practical applications for which the reference DNS solution is not available.

#### 4.4. Relevant length-scale for local error quantification

The error in the previous section is an integrated measure across the entire outer layer and, consistently, the grid resolution is non-dimensionalized by the boundary layer thickness  $\delta$ . However, the length-scale of the energy-containing eddies is a function of the wall-normal direction, and local errors at a given  $x_2$  are expected to vary accordingly. We investigate the physical length-scale relevant for local error scaling and define the  $x_2$ -dependent error in the mean velocity profile as

$$\mathcal{E}_{m,l}(x_2) = \left[ \frac{\frac{1}{2d} \int_{x_2-d}^{x_2+d} (\langle \tilde{u}_1 \rangle - \langle u_1 \rangle)^2 dx_2}{\frac{1}{0.8\delta} \int_{0.2\delta}^{\delta} \langle u_1 \rangle^2 dx_2} \right]^{1/2}, \quad (23)$$

where the integration limits,  $x_2 \pm d$ , coincide with the grid locations of  $\tilde{u}_1$ , and the integral is numerically performed using the trapezoidal rule. Different candidates for the normalization length-scale are tested, namely, the Kolmogorov scale  $\eta = (\nu^3/\varepsilon)^{1/4}$  [51], the Taylor microscale  $L_t = (15\nu\langle u'_i u'_i \rangle/\varepsilon)^{1/2}$  [77], the integral length-scale  $L_e = (K/3)^{3/2}/\varepsilon$  [51], and the shear length-scale  $L_s = u_\tau(\partial\langle u_1 \rangle/\partial x_2)^{-1}$  [78, 56], where  $\varepsilon$  is the rate of energy dissipation, and  $K$  is the turbulent kinetic energy. All the length-scales are computed for the reference DNS data. The results for AMD4200-EWS-i1,i2,i3,i4 are shown in Fig. 7, and similar results are obtained for the corresponding DSM cases. The best collapse is found for  $\Delta/L_s$ . The local error lies below 10% for  $\Delta < L_s$ , and it drastically drops for  $\Delta < 0.2L_s$ , although these ranges should be understood as tentative estimates. The largest errors are obtained for  $\Delta/L_s > 1$ , which corresponds to the grid points closer to the wall.

The scaling results for the local error  $\mathcal{E}_{m,l}$  are consistent with the excellent agreement in the global error  $\mathcal{E}_m$  when the grid resolutions are normalized by  $\delta$  (Fig. 4). The reason is that, at high  $Re_\tau$ , the universal shape of the mean velocity profile in the outer layer implies that the integrated effect of  $L_s$  is proportional to  $\delta$ . This can be easily seen by computing the average value of  $L_s$  for  $x_2 \in [0.2\delta, \delta]$  given by  $(L_s)_{avg} = 1/0.8\delta \int_{0.2\delta}^{\delta} L_s(x_2) dx_2 \sim \delta$ . Under the rough assumption that there is no wake effect and the log layer is valid until the edge of the boundary layer, then  $(L_s)_{avg} \approx 0.25\delta$ .

To conclude this section, we discuss one last interesting result regarding the local error at the  $n$ -th off-wall grid point. Considering that the  $n$ -th off-wall grid point is located at  $x_2 = n\Delta$ , and assuming that at high Reynolds numbers

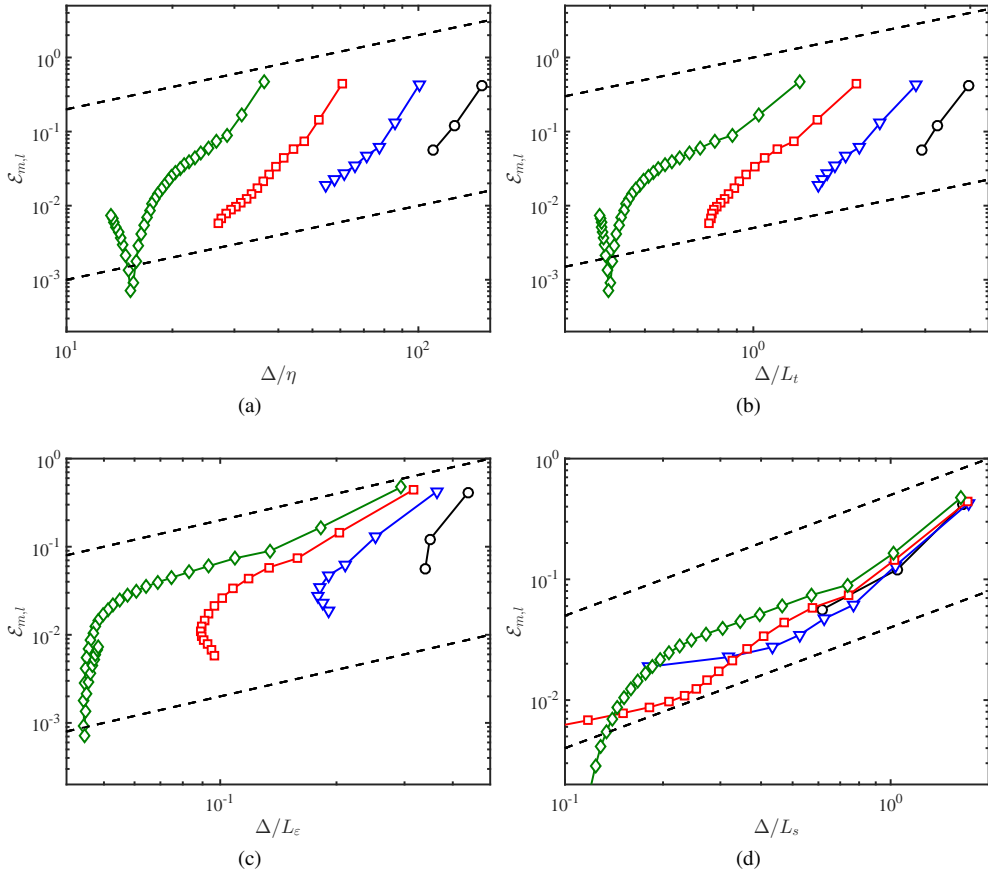


Fig. 7: Local error in the mean velocity profile  $\mathcal{E}_{m,l}$  as a function of the grid size  $\Delta$  normalized by (a) Kolmogorov scale  $\eta$ , (b) Taylor microscale  $L_t$ , (c) integral length-scale  $L_\varepsilon$ , and (d) shear length-scale  $L_s$ . Cases are AMD4200-EWS-i1 ( $\circ$ ), AMD4200-EWS-i2 ( $\nabla$ ), AMD4200-EWS-i3 ( $\square$ ), and AMD4200-EWS-i4 ( $\diamond$ ). The dashed lines in (d) are  $\mathcal{E}_{m,l} \sim \Delta/L_s$ .

the  $n$ -th point falls within the log layer (as expected in WMLES), then  $L_s \approx \kappa x_2$  and  $\Delta/L_s \approx 1/(n \cdot \kappa) \approx 2/n$  independently of  $\Delta$ . Consequently, no improved predictions are expected in  $\langle \tilde{u}_1 \rangle$  at the  $n$ -th off-wall grid point as  $\Delta$  is refined until the grid resolution reaches the WRLES-like regime. A similar argument was provided by Larsson et al. [79] based on the size of wall-attached eddies across the log layer.

## 5. Error scaling of turbulence intensities

In the previous section, we have measured the errors on  $\langle \tilde{u}_1 \rangle$  by assuming that LES and DNS are directly comparable. The assumption is reasonable if the filtering operation has a small impact on the mean of a variable  $\phi$ , that is,  $\langle \bar{\phi} \rangle \approx \langle \phi \rangle$ , which is the case for the mean velocity profile even at coarse filter sizes. However, smaller-scale motions play a non-negligible role in  $\langle u_i'^2 \rangle$ , casting doubts on how to compare fairly LES and DNS data. If LES is formally interpreted by means of a spatial low-pass filter [73, 3], the meaningful quantities to compare are the turbulence intensities of the filtered DNS velocities. There are two caveats in order to carry on such comparison. First, although numerical differentiation has a low-pass filtering effect and the finite grid resolution prevents the formation of small scales, the filter operator is not distinctly defined in implicitly-filtered LES [4, 5, 6, 7] and, consequently, neither is the associated filter size. The second caveat is probably more important: in real-world applications we are interested in predicting DNS values, whereas their filtered counterparts are of less practical importance. For these reasons, we study the error scaling of the LES fluctuating velocities with respect to unfiltered quantities.

In this section, we first argue that the physical mechanism regulating the magnitude of the fluctuating velocities in implicitly-filtered LES is not related to filtering, but rather to the requirement of generating velocity gradients

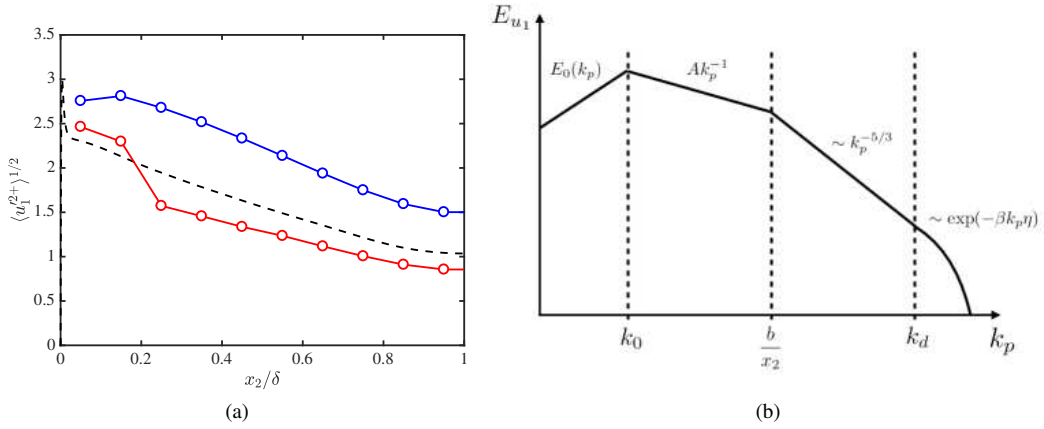


Fig. 8: (a) Streamwise r.m.s. velocity fluctuations for DNS at  $Re_\tau \approx 4200$  (---), NM4200-EWS-i2 ( $\circ$ ), and DSM4200-EWS-i2 ( $\circ$ ). (b) Model spectrum for the streamwise turbulence intensity. The parameters  $A$ ,  $b$ ,  $k_0$ ,  $k_d$  and  $\beta$  are model constants.

consistent with the statistically steady state. Secondly, we study the theoretical and numerical convergence of the LES turbulence intensities in wall-bounded flows.

### 5.1. The mechanism controlling fluctuating velocities in implicitly-filtered LES

Fig. 8(a) shows the root-mean-squared (r.m.s.) of the streamwise fluctuating velocity for DNS, LES without SGS model, and LES with DSM. In the absence of model, the LES intensities are over-predicted compared with DNS and, conversely, under-predicted with DSM. Similar results are obtained for the wall-normal and spanwise velocity fluctuations. The change in magnitude of the LES r.m.s. fluctuating velocities can be understood through the energy equation integrated over the channel flow domain  $\mathcal{V}$  with volume  $V$ ,

$$\frac{u_\tau^2 QV}{2\delta^2} = \int_{\mathcal{V}} (\nu + \nu_t) \left( \frac{\partial \tilde{u}_i}{\partial x_k} \frac{\partial \tilde{u}_i}{\partial x_k} + \frac{\partial \tilde{u}_i}{\partial x_k} \frac{\partial \tilde{u}_k}{\partial x_i} \right) dV. \quad (24)$$

Eq. (24) shows that the input power to maintain the mass flow  $Q$  must be dissipated by the viscous/SGS terms. In the DNS limit ( $\nu_t = 0$ ) with fixed  $\nu$ , this is achieved by the velocity gradients  $\partial \tilde{u}_i / \partial x_k \sim \Delta u_c / l_c$ , where  $\Delta u_c$  and  $l_c$  are the characteristic velocity difference and length of the smallest scales, respectively. In LES ( $\nu_t \neq 0$ ), the smallest available length-scale is limited by the grid resolution  $l_c \approx \Delta$ . Thus, the two possible mechanisms to maintain consistency with Eq. (24) are by  $\nu_t > 0$ , or by augmenting  $\Delta u_c$  (and hence the turbulence intensities). If  $\nu_t$  is large enough,  $\Delta u_c$  is under-predicted with respect to DNS as illustrated in Fig. 8(a). Conversely, if  $\nu_t$  is small, as in LES without explicit SGS model ( $\nu_t = 0$ ), the result is an increase of the turbulence intensities as shown in Fig. 8(a). This illustrates how the mean LES kinetic energy can exceed the mean DNS kinetic energy when SGS models are not dissipative enough (as in Fig. 6a), which may be problematic for LES quality assessment.

In summary, the physical mechanism regulating the magnitude of the fluctuating velocities in implicitly-filtered LES is related to the necessity of generating dissipative terms of the correct magnitude rather than by the (non-existent) filtering operation. Nevertheless, the results above shows that even if implicitly-filtered LES is not rigorously equivalent to the filtered Navier–Stokes equations, it does hold some resemblance in the sense that the values of  $\nu_t$  providing the correct mean velocity profile scaled by free stream, centerline, or bulk velocity, are accompanied by lower r.m.s. velocities as it would be expected from the filtered DNS velocity field.

### 5.2. Theoretical estimations

The metric adopted to measure errors in the turbulence intensities is

$$\mathcal{E}_{f,i} = \left[ \frac{\int_{0,2\delta}^{\delta} (\langle \tilde{u}_i'^2 \rangle - \langle u_i'^2 \rangle)^2 dx_2}{\int_{0,2\delta}^{\delta} \langle u_i'^2 \rangle^2 dx_2} \right]^{1/2}, \quad i = 1, 2, 3. \quad (25)$$

For brevity, we occasionally omit the subscript  $i$  when the particular flow component is not relevant in the discussion. Our goal is to estimate  $\mathcal{E}_f$  as a function of  $\Delta$ .

In the log layer of wall-bounded turbulence at high Reynolds numbers, the intensities of the unfiltered velocity fluctuations are known to follow

$$\frac{\langle u_1'^2 \rangle}{u_\tau^2} = B_1 - A_1 \log\left(\frac{x_2}{\delta}\right), \quad \frac{\langle u_2'^2 \rangle}{u_\tau^2} = B_2, \quad \frac{\langle u_3'^2 \rangle}{u_\tau^2} = B_3 - A_3 \log\left(\frac{x_2}{\delta}\right), \quad (26)$$

where the coefficients  $B_i$  and  $A_i$  are constants considered to be universal for turbulent channel flows. Eq. (26) can be derived by using the attached-eddy hypothesis [80] or by dimensional analysis on the  $k^{-1}$  spectrum of  $u_1$  and  $u_3$  [52], and the blocking effect of the wall for  $u_2$ . The hypothesis has been confirmed at high Reynolds number flows [81, 82] and it has also been observed in the spanwise velocity even for relatively low Reynolds numbers [83, 84, 85, 86]. An important consequence of Eq. (26) is that, at a given  $x_2/\delta$ , the magnitude of the velocity fluctuations scaled by  $u_\tau$  is constant and independent of the Reynolds number.

We are now interested in the LES asymptotic high-Reynolds-number limit for the filtered fluctuating velocities  $\langle \bar{u}_i'^2 \rangle$ ,

$$\frac{\langle \bar{u}_1'^2 \rangle}{u_\tau^2} = \bar{B}_1 - \bar{A}_1 f\left(\frac{x_2}{\delta}\right), \quad \frac{\langle \bar{u}_2'^2 \rangle}{u_\tau^2} = \bar{B}_2, \quad \frac{\langle \bar{u}_3'^2 \rangle}{u_\tau^2} = \bar{B}_3 - \bar{A}_3 f\left(\frac{x_2}{\delta}\right), \quad (27)$$

where  $\bar{B}_i$  and  $\bar{A}_i$  are constants that depend on  $\Delta_i$ , and  $f$  is an unknown function such that  $f(x_2) \rightarrow \log(x_2)$  as  $\Delta_i \rightarrow 0$ . The exact dependence of  $\bar{B}_i$ ,  $\bar{A}_i$  on  $\Delta_i$ , and the particular shape of  $f$  is expected to vary for different filter kernels. The value of  $\langle \bar{u}_i'^2 \rangle$  may be estimated for a symmetric filter with well-defined, non-zero second moment in real space by considering [5, 70]

$$\langle \bar{u}_i'^2 \rangle = \langle \overline{u_i'^2} \rangle - \Delta_k^2 \left\langle \left( \frac{\partial \bar{u}_i'}{\partial x_k} \right)^2 \right\rangle + \mathcal{O}(\Delta_1^4 + \Delta_2^4 + \Delta_3^4). \quad (28)$$

If we further assume that  $\langle \overline{u_i'^2} \rangle \approx \langle u_i'^2 \rangle$ , then

$$\frac{\langle \bar{u}_i'^2 \rangle}{u_\tau^2} = B_i - A_i \log\left(\frac{x_2}{\delta}\right) - \Delta_k^2 \left\langle \left( \frac{\partial \bar{u}_i'}{\partial x_k} \right)^2 \right\rangle + \mathcal{O}(\Delta_1^4 + \Delta_2^4 + \Delta_3^4), \quad (29)$$

where  $A_2 = 0$ . Eq. (29) shows that the wall-parallel turbulence intensities of the filtered field do not follow Eq. (26), and the major contributor to the departure from the classic log-law is the correction term on the right-hand side of Eq. (29). The error is then given by

$$\mathcal{E}_f \sim \Delta_k^2 \left\langle \left( \frac{\partial \bar{u}_i'}{\partial x_k} \right)^2 \right\rangle. \quad (30)$$

Equation (30), together with the estimations for the velocity gradient  $G$  in Section 4.1, yields

$$\mathcal{E}_f^s \sim \Delta^0, \quad \mathcal{E}_f^i \sim \Delta^{2/3}, \quad (31)$$

which predict a low convergence rate of the LES turbulence intensities for  $\Delta$  comparable to the scales in shear-dominated regime ( $\mathcal{E}_f^s$ ), and in the inertial range ( $\mathcal{E}_f^i$ ).

A limitation of Eq. (31) is that it does not provide any insight into the explicit logarithmic dependence of  $\langle u_1'^2 \rangle$  and  $\langle u_3'^2 \rangle$  with  $x_2$ . An alternative procedure to estimate  $\mathcal{E}_f$  is to connect Eq. (26) and Eq. (27) by the spectrum of the streamwise velocity,

$$\frac{\langle u_1'^2 \rangle}{u_\tau^2} = 2 \int_0^\infty E_{u_1}(k_p, x_2) dk_p, \quad (32)$$

where  $E_{u_i}$  is the two-dimensional spectrum for the  $i$ -th velocity component as a function of  $k_p^2 = k_1^2 + k_3^2$ , where  $k_1$  and  $k_3$  are the streamwise and spanwise wavenumbers, respectively. Similarly,

$$\frac{\langle \bar{u}_i'^2 \rangle}{u_\tau^2} = 2 \int_0^\infty \bar{E}_{u_i}(k_p, x_2) dk_p, \quad (33)$$

where  $\bar{E}_{u_i}(k_p, x_2)$  is the energy spectra of the filtered velocities. We focus on the streamwise velocity component, but the reasoning below is also applicable to the spanwise component. To make the problem tractable, we adopt the model spectrum for  $E_{u_1}$  from Fig. 8(b). The four different piecewise domains of the model correspond to the large-scale, shear-dominated [52], inertial [72], and viscous regimes [87], respectively. Evaluation of Eq. (32) using the model from Fig. 8(b) results in

$$\frac{\langle u_1'^2 \rangle}{2u_\tau^2} \approx \text{constant} - A \log\left(\frac{x_2}{b}\right), \quad (34)$$

where the contributions from inertial and viscous regimes have been neglected. The result is consistent with the logarithmic functional dependence of the streamwise turbulence intensity from Eq. (26). Under the severe assumptions that the filtering operator resembles a sharp Fourier cut-off, and neglecting filtering in the wall-normal direction,

$$\frac{\langle \bar{u}_1'^2 \rangle}{u_\tau^2} = 2 \int_0^\infty \bar{E}_{u_1}(k_p, x_2) dk_p \approx 2 \int_0^{\pi/\Delta} E_{u_1}(k_p, x_2) dk_p. \quad (35)$$

The difference  $\langle u_1'^2 \rangle - \langle \bar{u}_1'^2 \rangle$  defintory of the error in Eq. (25) is

$$\mathcal{E}_f \sim \int_0^\infty E_{u_1}(k_p, x_2) dk_p - \int_0^{\pi/\Delta} E_{u_1}(k_p, x_2) dk_p, \quad (36)$$

and after integration we obtain

$$\mathcal{E}_f^s \sim \log(\Delta/x_2), \quad \mathcal{E}_f^i \sim \Delta^{2/3}. \quad (37)$$

When the filter cut-off lies within the  $k_p^{-1}$  regime, Eq. (37) predicts a  $\log(\Delta/x_2)$  correction to the  $\Delta^0$ -dependence estimated in Eq. (31), although both cases imply a slow convergence with  $\Delta$ . Regarding the behavior of  $\langle \bar{u}_1'^2 \rangle$ , for  $\Delta$  within the shear-dominated region,

$$\langle \bar{u}_1'^2 \rangle \approx \text{constant} + \mathcal{O}(\log(\Delta)), \quad (38)$$

and the LES streamwise and spanwise turbulence intensities will not reproduce the asymptotic logarithmic profile. For the inertial range, the prediction of Eq. (37) coincides with the one reported in Eq. (31). In this case, integration of the model spectrum yields

$$\langle \bar{u}_1'^2 \rangle \approx \text{constant} - A \log(x_2) + \mathcal{O}(\Delta^{2/3}), \quad (39)$$

and LES is expected to capture the classic logarithmic behavior in  $x_2$  with a correction of the order of  $\Delta^{2/3}$ .

### 5.3. Numerical assessment

We aim to quantify the exponents  $\alpha_f$  and  $\gamma_f$  for

$$\mathcal{E}_f \sim \left(\frac{\Delta}{\delta}\right)^{\alpha_f} Re_\tau^{\gamma_f}, \quad (40)$$

from LES data and the range of grid resolutions of interest in the present work. The results reported in this section are strictly valid for LES with DSM. Nevertheless, similar conclusions are drawn for AMD and  $x_2 > 0.3\delta$ , where the turbulence intensities predicted by AMD and DSM are almost indistinguishable. The results are also compared with filtered DNS data (fDNS), but this is only done qualitatively. For that, we use a three-dimensional box-filter with filter size equal to the LES grid resolution in each direction. The choice of this particular filter shape and filter size is arbitrary, and it is argued before that no specific form can be established *a priori* for implicitly-filtered LES.

Figs. 9(a)–(c) show the turbulence intensities as a function of the wall-normal distance for DNS and LES at  $Re_\tau \approx 2000$  and various grid resolutions. The main observation from Fig. 9(a) is that the LES turbulence intensities diverge from DNS as the grid is coarsened, and the shape of the  $\langle \bar{u}_i'^2 \rangle$  becomes distinctively different from  $\langle u_i'^2 \rangle$ . Moreover, the effect is more pronounced closer to the wall. Hence, the logarithmic behavior is not captured by LES when  $\Delta = \mathcal{O}(\delta)$ , consistent with the discussion in Section 5.2. The error between LES and DNS is quantified in Fig.



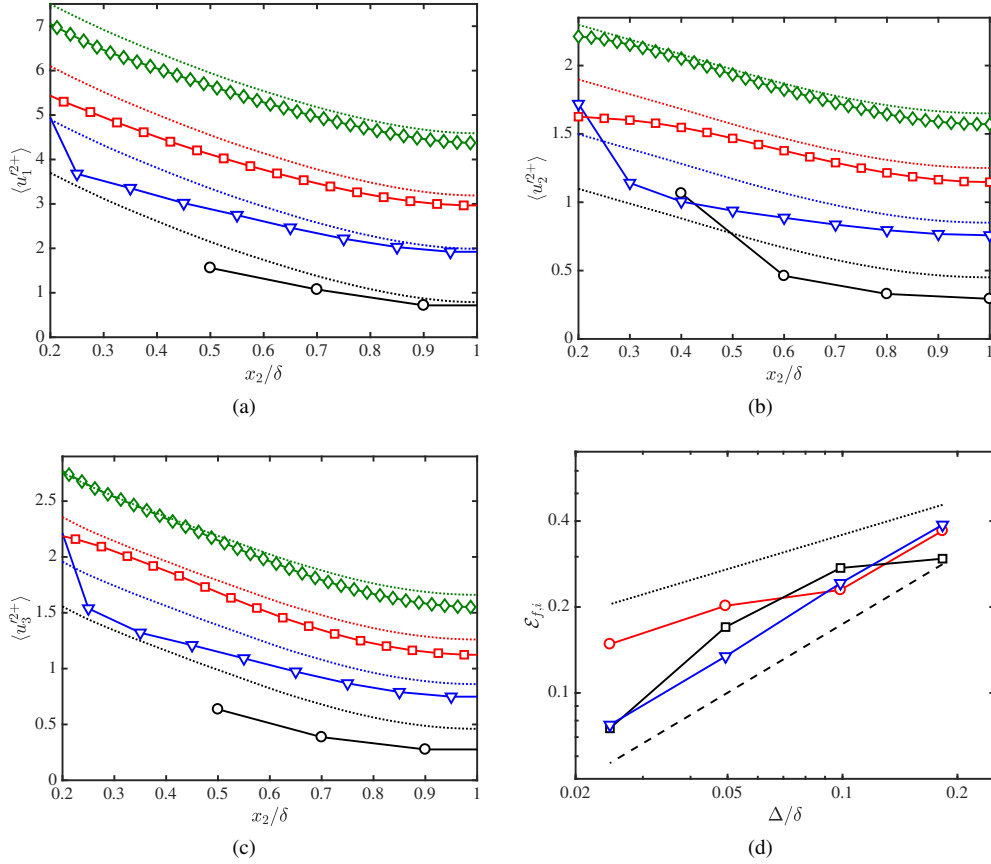


Fig. 9: Streamwise (a), wall-normal (b), and spanwise (c) turbulence intensities as a function of the wall-normal distance for different grid resolutions at  $Re_\tau \approx 2000$ . Symbols are LES cases DSM2000-EWS-i1 ( $\circ$ ), DSM2000-EWS-i2 ( $\nabla$ ), DSM2000-EWS-i3 ( $\square$ ), DSM2000-EWS-i4 ( $\diamond$ ). For clarity, cases DSM2000-EWS-i2, DSM2000-EWS-i3 and DSM2000-EWS-i4 are vertically shifted by 1.2, 2.4 and 3.8 wall units, respectively. For comparison, each LES case is accompanied by DNS data (-----) vertically shifted by the same amount. The first two points closer to the wall for case DSM2000-EWS-i1 are omitted as they are contaminated by the nonphysical solution close to the wall. (d) Error in the streamwise  $\mathcal{E}_{f,1}$  ( $\circ$ ), wall-normal  $\mathcal{E}_{f,2}$  ( $\square$ ), and spanwise  $\mathcal{E}_{f,3}$  ( $\nabla$ ) turbulence intensities as a function of the characteristic grid resolution. The dashed and dotted lines are  $\mathcal{E}_f \sim \Delta^{0.8}$  and  $\mathcal{E}_f \sim \Delta^{0.4}$ , respectively.

9(d) and compared with the predictions from Eq. (31). The results show that  $\mathcal{E}_{f,1}$  converges as  $\Delta^{0.4}$ , whereas  $\mathcal{E}_{f,2}$  and  $\mathcal{E}_{f,3}$  are well represented by  $\Delta^{0.8}$ .

The effect of the Reynolds number is evaluated in Fig. 10, which also includes comparisons with fDNS. The grid resolution (or filter size) for the LES and fDNS cases is set to i2 from Table 2 ( $\Delta = 0.1\delta$ ), and  $Re_\tau$  ranges from  $\approx 950$  to  $\approx 4200$ . The dependence of  $\mathcal{E}_{f,i}$  with  $Re_\tau$  is weak, and the error remains roughly constant for  $Re_\tau > 950$ , from where we conclude that  $\gamma_f \approx 0$ . Therefore, the empirically measured error for the LES turbulence intensities scales as

$$\mathcal{E}_{f,1} \sim \left(\frac{\Delta}{\delta}\right)^{0.4} Re_\tau^0, \quad \mathcal{E}_{f,2/3} \sim \left(\frac{\Delta}{\delta}\right)^{0.8} Re_\tau^0, \quad (41)$$

for  $\Delta > 0.025\delta$ . The empirical results in Eq. (41) corroborate that the correct representation of  $\langle \overline{u_i'^2} \rangle$  is more demanding than that for the mean velocity profile, consistent with the analysis in Section 5.2. The results are closer to the theoretical error prediction obtained for  $\Delta$  comparable to the inertial length-scales ( $\mathcal{E}_f^i \sim \Delta^{2/3}$ ), albeit the convergence rate for  $\mathcal{E}_{f,1}$  is more moderate than for  $\mathcal{E}_{f,2}$  and  $\mathcal{E}_{f,3}$ . Nonetheless, we have discussed before that the error estimations from theoretical arguments presented above should be appraised as indicative of the actual non-linear error rather than as strict error laws.

Fig. 10(a) also shows that the LES turbulence intensities are well approximated by fDNS, especially for the highest

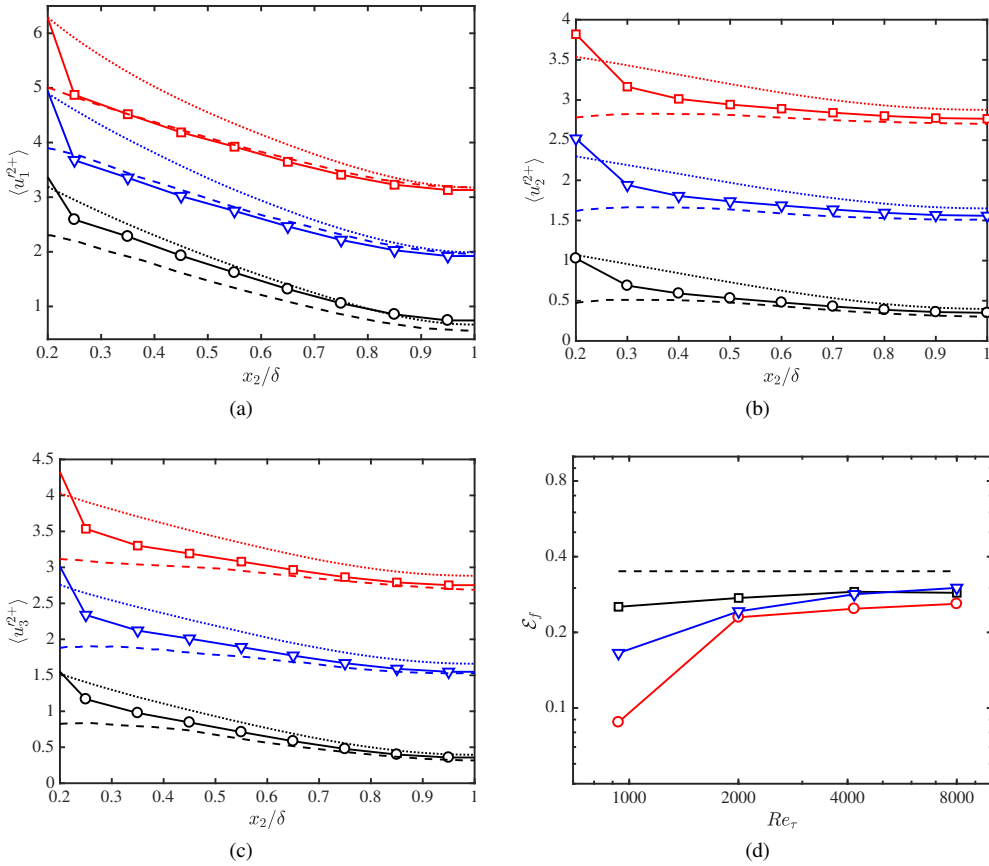


Fig. 10: Streamwise (a), wall-normal (b), and spanwise (c) turbulence intensities as a function of the wall-normal distance for different Reynolds numbers with grid resolution i2. Symbols are LES cases DSM950-EWS-i2 ( $\circ$ ), DSM2000-EWS-i2 ( $\nabla$ ), and DSM4200-EWS-i2 ( $\square$ ). For clarity, cases DSM2000-EWS-i2 and DSM4200-EWS-i2 are vertically shifted by 1.2 and 2.4 wall units, respectively. For comparison, each LES case is accompanied by DNS data ( $\cdots$ ) and box filtered DNS data ( $---$ ) vertically shifted by the same amount. (d) Error in the streamwise  $\mathcal{E}_{f,1}$  ( $\circ$ ), wall-normal  $\mathcal{E}_{f,2}$  ( $\square$ ), and spanwise  $\mathcal{E}_{f,3}$  ( $\nabla$ ) turbulence intensities as a function of the Reynolds number. The dashed line is  $\mathcal{E}_f = 0.35$ .

Reynolds numbers and far from the wall. We have argued at the beginning of the section that the filter operator is not well-defined in implicitly-filtered LES, and the results here should be interpreted only as an indication that the LES fluctuating velocities are comparable to filtered DNS values when the filter size is appropriately chosen.

Similarly to the mean velocity profile, the error from Eq. (25) can be re-evaluated locally along different wall-normal bands to explore the relevant physical scale-length to refer  $\Delta$ . We define the local error for the turbulent kinetic energy  $K = (u_1'^2 + u_2'^2 + u_3'^2)/2$  (analogously for LES) as

$$\mathcal{E}_{K,l}(x_2) = \left[ \frac{\frac{1}{2d} \int_{x_2-d}^{x_2+d} (\langle \bar{K} \rangle - \langle K \rangle)^2 dx_2}{\frac{1}{0.8\delta} \int_{0.2\delta}^{\delta} \langle K \rangle^2 dx_2} \right]^{1/2}, \quad (42)$$

which is numerically computed as Eq. (23). Results from Fig. 11 show that  $\mathcal{E}_{K,l} \sim (\Delta/L_s)^{2/3}$ , and the shear length-scale  $L_s$  stands again as a sensible measure of the size of the energy-containing eddies relevant for quantifying LES errors. The collapse obtained by scaling the grid resolution by  $L_\varepsilon$ ,  $\eta$  and  $L_t$  is less satisfactory, and the last two are not shown.

For completeness, we also consider the interpretation of  $\langle u_i' u_j' \rangle$  as a Reynolds stress tensor instead of as a velocity variance. In the former case,

$$R_{ij}^{DNS} = \langle u_i' u_j' \rangle = \langle u_i u_j \rangle - \langle u_i \rangle \langle u_j \rangle, \quad (43)$$

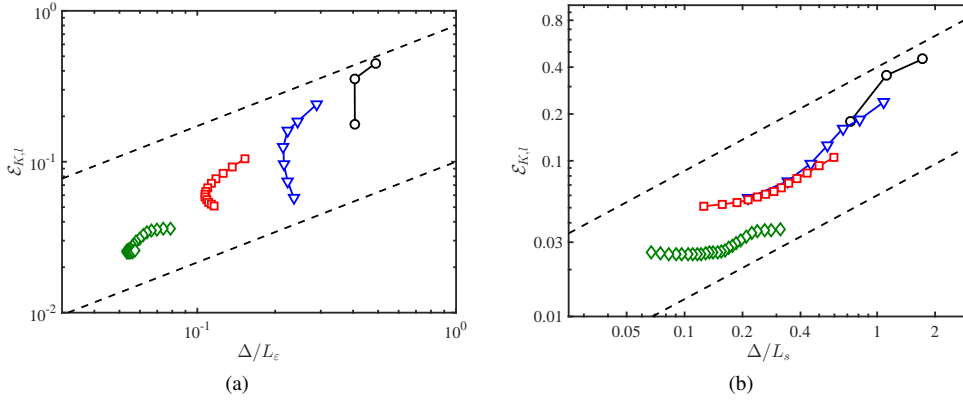


Fig. 11: Local error in the turbulence kinetic energy  $\mathcal{E}_{K,l}(x_2)$  as a function of  $\Delta$  normalized by (a)  $L_\epsilon$  and (b)  $L_s(x_2)$ . Colors represent different grid resolutions from Table 2: i1 (black, DSM2000-EWS-i1), i2 (blue, DSM2000-EWS-i2), i3 (red, DSM2000-EWS-i3), and i4 (green, DSM2000-EWS-i4). Dashed lines are (a)  $\mathcal{E}_{K,l} = 0.2(\Delta/L_\epsilon)^{2/3}$  and  $\mathcal{E}_{K,l} = 1.2(\Delta/L_\epsilon)^{2/3}$ , and (b)  $\mathcal{E}_{K,l} = 0.4(\Delta/L_s)^{2/3}$ .

where the diagonal components of  $R_{ij}^{\text{DNS}}$  are the mean squared DNS velocity fluctuations. As argued in Carati et al. [5], assuming  $\langle \tilde{\phi} \rangle \approx \langle \phi \rangle$ ,

$$R_{ij}^{\text{DNS}} = \langle u_i u_j \rangle - \langle u_i \rangle \langle u_j \rangle \approx \langle \overline{u_i u_j} \rangle - \langle \overline{u_i} \rangle \langle \overline{u_j} \rangle \approx \langle \tilde{u}_i \tilde{u}_j \rangle + \langle \tau_{ij}^{\text{SGS}} \rangle - \langle \tilde{u}_i \rangle \langle \tilde{u}_j \rangle = R_{ij}^{\text{LES}}. \quad (44)$$

Thus, the main difference between considering  $\langle u_i' u_j' \rangle$  as a stress rather than a velocity variance lies on the contribution of the SGS tensor. An advantage of Eq. (44) is that  $R_{ij}^{\text{DNS}}$  and  $R_{ij}^{\text{LES}}$  are directly comparable without prescribing a particular filtering operation. However, the approach is also accompanied by a limitation for the incompressible Navier–Stokes equations, where only the traceless part of  $\tau_{ij}^{\text{SGS}}$  is modeled. Hence, in order to allow for straight comparisons only the deviatoric contributions of  $R_{ij}^{\text{DNS}}$  and  $R_{ij}^{\text{LES}}$  must be taken into consideration [88]. An error analogous to Eq. (25) can be defined using the traceless counterparts of  $R_{ij}^{\text{DNS}}$  and  $R_{ij}^{\text{LES}}$ . The results, omitted for brevity, show that the errors have a weak dependence on the grid resolution and follow  $\sim (\Delta/\delta)^{\alpha_f}$ , with  $\alpha_f < 2/3$ .

## 6. Error scaling of the velocity spectra

We consider the two-dimensional kinetic energy spectrum for the unfiltered velocity field at a given wall-normal distance  $x_2$ ,  $E_K(k_1, k_3, x_2) = \langle \hat{u}_i \hat{u}_i^* \rangle_t / 2$ , where  $\widehat{(\cdot)}$  is the Fourier transform in the homogeneous directions,  $(\cdot)^*$  denotes complex conjugate, and  $\langle \cdot \rangle_t$  is average in time. Similarly, the kinetic energy spectrum for the LES velocity is  $\tilde{E}_K(k_1, k_3, x_2) = \langle \tilde{u}_i \tilde{u}_i^* \rangle_t / 2$ . The magnitude of  $E_K$  is given by

$$\langle u_1'^2 + u_2'^2 + u_3'^2 \rangle = 2 \int_0^\infty \int_0^\infty E_K(k_1, k_3, x_2) dk_1 dk_3, \quad (45)$$

(analogously for  $\tilde{E}_K$ ) and it was investigated in the previous section. We are now interested in accuracy of LES to predict the distribution of energy in the homogeneous scale-space at a given wall-normal distance. The error in the energy spectrum is defined as

$$\mathcal{E}_s(x_2) = \left[ \left\langle \left( \tilde{E}_K - E_K \right)^2 \right\rangle_{k_1, k_3} \right]^{1/2}, \quad (46)$$

where  $\langle \cdot \rangle_{k_1, k_3}$  denotes average over the wall-parallel wavenumbers. Again, we are concerned with the error of LES compared to unfiltered DNS.

### 6.1. Theoretical estimations

The effect of  $\tau_{ij}$  on the distribution of energy can be analyzed by considering the spectral kinetic energy equation for  $\tilde{E}_K$  at a given wall-normal distance,

$$\frac{\partial \tilde{E}_K}{\partial t} = \hat{P} + \hat{T} + \hat{\Pi} + \hat{D} + \hat{\varepsilon} + \hat{D}_\tau + \hat{\varepsilon}_\tau, \quad (47)$$

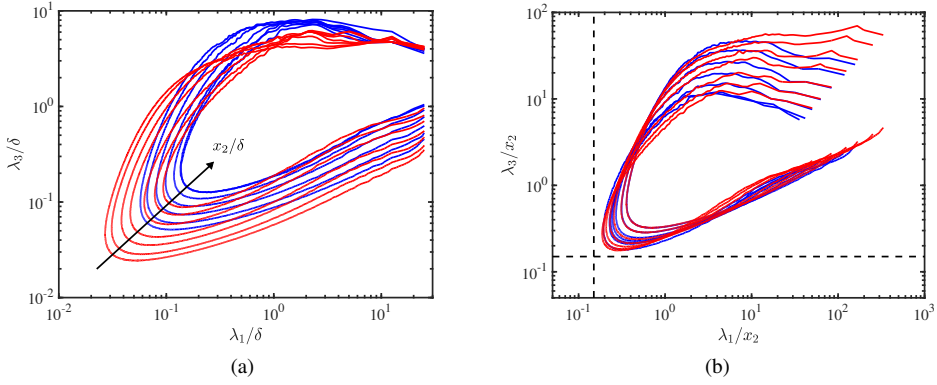


Fig. 12: Premultiplied two-dimensional kinetic energy spectra for DNS data as a function of the streamwise ( $\lambda_1$ ) and spanwise ( $\lambda_3$ ) wavelengths normalized by (a)  $\delta$ , and (b) wall-normal distance  $x_2$ . Colors are blue for  $Re_\tau \approx 950$  and red for  $Re_\tau \approx 2000$ . Different contours denote different wall-normal heights  $x_2/\delta = 0.16, 0.21, 0.30, 0.40, 0.50$  and  $0.60$  for  $Re_\tau \approx 950$ , and  $x_2/\delta = 0.08, 0.10, 0.15, 0.20, 0.30, 0.40$  and  $0.50$  for  $Re_\tau \approx 2000$ . Contours contain 90% of the turbulent kinetic energy. The straight dashed lines in (b) are  $\lambda_1/x_2 = 0.15$  and  $\lambda_3/x_2 = 0.15$ .

where the first five terms on the right-hand are the production rate of the turbulent kinetic energy ( $\hat{P}$ ), turbulent transport ( $\hat{T}$ ), pressure diffusion ( $\hat{\Pi}$ ), viscous diffusion ( $\hat{D}$ ), and the molecular dissipation rate ( $\hat{\epsilon}$ ), respectively. The explicit form of these terms can be found in Mizuno [89]. We focus on the contributions from  $\tau_{ij}$ ,

$$\hat{\epsilon}_\tau = \mathbb{R} \left[ -\sqrt{-1}k_1 \langle \hat{u}_i^* \hat{\tau}_{i1} \rangle_t - \sqrt{-1}k_3 \langle \hat{u}_i^* \hat{\tau}_{i3} \rangle_t + \left\langle \frac{\partial \hat{u}_i^*}{\partial x_2} \hat{\tau}_{i2} \right\rangle_t \right], \quad \text{and} \quad \hat{D}_\tau = \mathbb{R} \left[ -\frac{\partial \langle \hat{\tau}_{i2} \hat{u}_i^* \rangle_t}{\partial x_2} \right], \quad (48)$$

where  $\mathbb{R}$  denotes real part. The term  $\hat{\epsilon}_\tau$  is the dissipation rate of the spectral kinetic energy by  $\tau_{ij}$ , while  $\hat{D}_\tau$  is the wall-normal turbulent transport by  $\tau_{ij}$ . A detailed equation for the spectral error can be derived from Eq. (47) although the result is quite cumbersome. Instead, we assume by dimensional arguments that the functional dependence of  $\mathcal{E}_s$  on  $\Delta$  is proportional to the temporal integration of  $(\hat{\epsilon}_\tau + \hat{D}_\tau)$ ,

$$\mathcal{E}_s \sim \int_0^{t_c} (\hat{\epsilon}_\tau + \hat{D}_\tau) dt \sim \Delta^2 G, \quad (49)$$

where  $t_c \sim G^{-1}$  is the characteristic time-scale for the evolution of the eddies of size  $\Delta$ , and  $G$  is the characteristic velocity gradient. The estimated errors scale as

$$\mathcal{E}_s^s \sim \Delta, \quad \mathcal{E}_s^i \sim \Delta^{4/3} \quad (50)$$

for grid resolutions comparable to the eddies in the shear-dominated ( $\mathcal{E}_s^s$ ) or inertial ( $\mathcal{E}_s^i$ ) range, respectively.

## 6.2. Energy-resolving grid resolution estimations

Prior to the numerical assessment of the error scaling, we estimate the required LES grid resolution to resolve 90% of the turbulent kinetic energy at a given wall-normal distance. To that end, we use the two-dimensional spectral energy density  $E_K(\lambda_1, \lambda_3, x_2)$  as a function of the streamwise and spanwise wavelengths, namely  $\lambda_1 = 2\pi/k_1$  and  $\lambda_3 = 2\pi/k_3$ , respectively. Simple models describing the two-dimensional energy spectral at moderate and high Reynolds numbers have been proposed by Del Álamo et al. [90] and Chandran et al. [91], respectively. However, both works focus on the energy bounds for the large scales, whereas we are interested in the limiting length-scales for the smaller energy-containing eddies; that is, we are seeking for the minimum streamwise and spanwise grid spacing,  $\Delta_1^{\min}$  and  $\Delta_3^{\min}$  such that  $E_K(\lambda_1 > 2\Delta_1^{\min}, \lambda_3 > 2\Delta_3^{\min}, x_2)$  contains 90% of the total turbulent kinetic energy. Fig. 12(a) shows iso-contours of  $E_K$  enclosing 90% of the energy at difference wall-normal distances. As expected, the size of the energy-containing eddies decreases as they get closer to the wall. As postulated by the attached-eddy hypothesis [80] [see also 92, for a review], the only relevant length-scales for the energy-containing motions spanning along the log layer is  $x_2$ , which allows to write the energy spectra as

$$E_K = E_K(\lambda_1/x_2, \lambda_3/x_2). \quad (51)$$

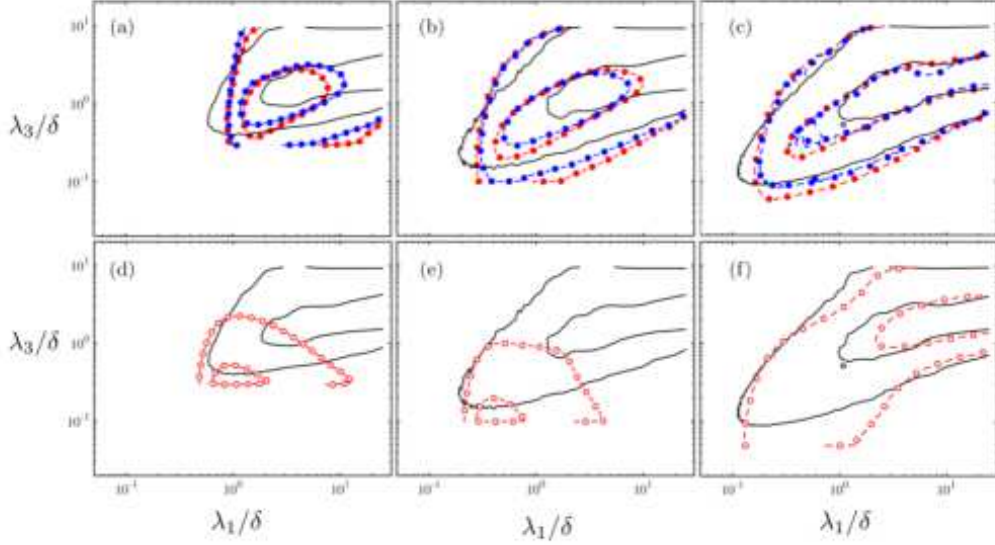


Fig. 13: Premultiplied two-dimensional streamwise velocity spectra as a function of the streamwise ( $\lambda_1$ ) and spanwise ( $\lambda_3$ ) wavelengths at  $x_2 = 0.75\delta$  for different grid resolutions from Table 2. (a,d) i1 ( $\Delta = 0.2\delta$ ), (b,e) i3 ( $\Delta = 0.05\delta$ ), (c,f) i4 ( $\Delta = 0.025\delta$ ). Colors and symbols are DSM ( $\bullet$ ), AMD ( $\bullet$ ), and no explicit SGS model ( $\circ$ ). Solid lines represent box filtered DNS data. Contours are 0.1 and 0.6 of the maximum.

The proportionality of the sizes of eddies with the wall-normal distance was originally hypothesized as an asymptotic limit at very high Reynolds numbers and used in the classical derivation of the logarithmic velocity profile [93], but it has been observed experimentally and numerically in spectra and correlations at relatively modest Reynolds numbers in pipes [94, 95, 52, 96, 97, 98, 99] and in turbulent channels and flat-plate boundary layers [100, 90, 67, 101, 102, 38, 56]. The performance of the scaling from Eq. (51) for DNS channel flows is shown in Fig. 12(b) for various heights and Reynolds numbers. The results demonstrate the improved collapse of the kinetic energy spectra, and enables the estimation of energy bounds that are approximately valid at all the wall-normal distances within the outer layer. Taking  $(\lambda_1)_{\min} = 2\Delta_1^{\min}$  and  $(\lambda_3)_{\min} = 2\Delta_3^{\min}$ , the *a priori* minimum wall-parallel grid resolutions to resolve 90% of the turbulent kinetic energy at  $x_2$  are roughly given by

$$\left(\frac{\lambda_1}{x_2}\right)_{\min} = \frac{2\Delta_1^{\min}}{x_2} \approx 0.15, \quad \left(\frac{\lambda_3}{x_2}\right)_{\min} = \frac{2\Delta_3^{\min}}{x_2} \approx 0.15. \quad (52)$$

The limit 0.15 was estimated from the dashed straight lines in Fig. 12(b), which bound the contours containing 90% of the turbulent kinetic energy. For example, to resolve 90% of the turbulent kinetic energy at  $x_2 \approx 0.5\delta$ , we require  $\Delta_1 = \Delta_3 \approx 0.04\delta$ . These estimates were used in Section 4.2 to explain the observations in Fig. 5. The grid resolution guidelines in Eq. (52) imply that  $\Delta_1 \approx \Delta_3$ , in contrast with the common choice of  $\Delta_1 > \Delta_3$  among LES practitioners, and usually argued in terms of the elongated streamwise velocity streaks typical of wall-bounded flows. However, it is clear from Fig. 12(b) that the ‘nose’ of the energy spectra is located at  $\lambda_1 \approx \lambda_3$ , which justifies the choice of  $\Delta_1 \approx \Delta_3$ . For coarser grid resolutions aiming to resolve a lower fraction of the turbulent kinetic energy, it is then reasonable to choose  $\Delta_1 > \Delta_3$ .

### 6.3. Numerical assessment

Fig. 13 displays the premultiplied two-dimensional spectra of the streamwise velocity for fDNS and LES (with DSM, AMD, and no explicit SGS model). The filtered spectra was calculated from box-filtered DNS data with a filter size  $\Delta_1 \times \Delta_2 \times \Delta_3$ . The results show that both DSM and AMD perform similarly, and that the LES spectra is representative of the expected energy distribution for the filtered velocities (Figs. 13a-c), although the LES prediction tends to be biased towards smaller scales for all grid resolutions.

For cases without explicit SGS model, the spectra is seriously misrepresented for  $\Delta > 0.05\delta$  (Figs. 13d-e), with most of the energy piled up close to the smallest scales supported by the grid. The physical interpretation of this

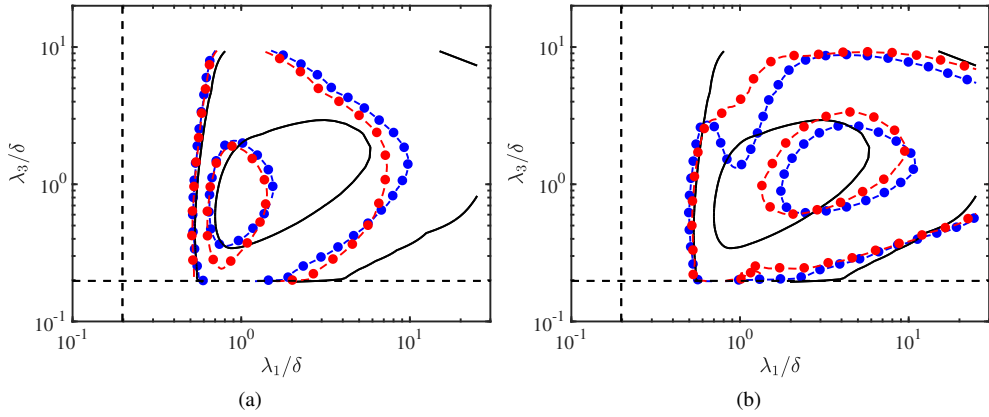


Fig. 14: Premultiplied two-dimensional spectra of the turbulent kinetic energy  $\tilde{E}_K$  (—) compared with (a) the SGS dissipation rate of spectral kinetic energy  $\hat{\varepsilon}_{SGS}$  (closed circles), and (b) the SGS turbulent transport  $\hat{D}_{SGS}$  (closed circles) as function of the streamwise ( $\lambda_1$ ) and spanwise ( $\lambda_3$ ) wavelengths at  $x_2 = 0.75\delta$ . Symbols are (●) for DSM2000-EWS-i2, and (●) for AMD2000-EWS-i2. Contours are 0.1 and 0.6 of the maximum of  $\tilde{E}_K$ ,  $\hat{D}_{SGS}$ , and  $|\hat{\varepsilon}_{SGS}|$  for each quantity, respectively. The dashed lines are  $\lambda_1/\delta = \lambda_3/\delta = 0.2$ .

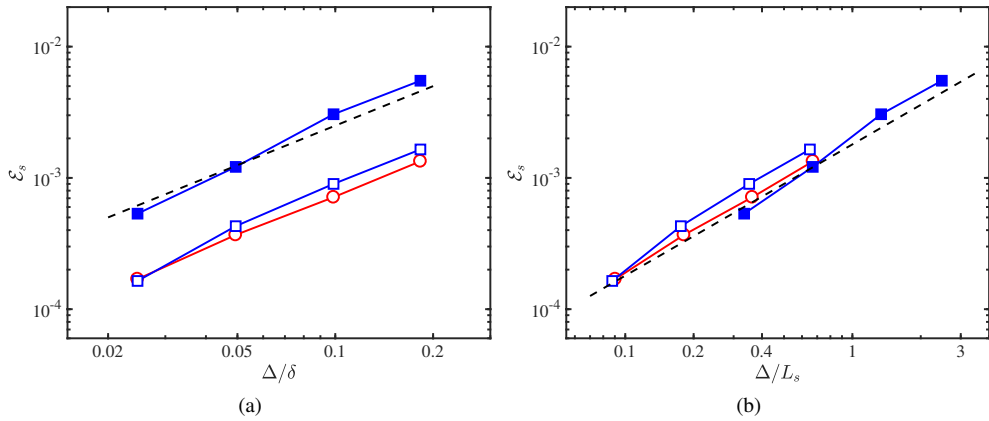


Fig. 15: Error in the kinetic energy spectra  $\mathcal{E}_s$  as a function of the characteristic grid size  $\Delta$  scaled by (a)  $\delta$ , and (b)  $L_s(x_2)$ . Open symbols are for  $x_2 = 0.75\delta$ , and closed symbols for  $x_2 = 0.2\delta$ . Colors are red for  $Re_\tau \approx 950$ , and blue for  $Re_\tau \approx 2000$ . Results are for LES with DSM. The dashed line is (a)  $\mathcal{E}_s \sim (\Delta/\delta)^{4/3}$  and (b)  $\mathcal{E}_s \sim (\Delta/L_s)^{4/3}$ .

effect was provided in Section 5.1 in terms of the necessary velocity gradients to comply with the conservation of energy. Figs. 13(d)-(e) are just the spectral depiction of the same effect, i.e., the energy cascades towards the smallest available scales until the resulting gradients can balance the input power driving the channel. The distribution of energy changes drastically for  $\Delta < 0.05\delta$ , where large-scale streaks are now a clear constituent feature of the flow (Fig. 13f). The result is consistent with the visualizations in Fig. 5(d), which shows a clear streaky pattern in the streamwise velocity for  $\Delta = 0.025\delta$ , but a notably different non-streaky structure for  $\Delta > 0.05\delta$ . The existence of this critical grid resolution may be connected to the grid requirements estimated in Section 6.2, where it was concluded that  $\Delta \approx 0.04\delta$  in order to capture at least 90% of the turbulent kinetic energy at  $x_2 \approx 0.5\delta$ . This seems to be a necessary requirement to support the development of streaks in the absence of SGS model, at least for the particular numerical discretization adopted in this study.

Two mechanisms are potentially responsible for the improvements reported in Fig. 13 for cases with SGS model: the dissipation of the energy piled up at the smallest LES scales by  $\hat{\varepsilon}_{SGS}$ , and the redistribution of energy in the wall-normal direction by  $\hat{D}_{SGS}$ . These are the LES counterparts of  $\hat{\varepsilon}_\tau$  and  $\hat{D}_\tau$  discussed in Section 6.1 and their spectra are plotted in Fig. 14. The computed values reveal that the main contributor is  $\hat{\varepsilon}_{SGS}$  whose magnitude is roughly ten times larger than that of  $\hat{D}_{SGS}$ . Hence, the improved predictions of the velocity spectra in Fig. 13(a) and (b) are mostly due to the removal of the excess of energy close to the grid cut-off.

Finally, the scaling of  $\mathcal{E}_s$  is evaluated in Fig. 15 using LES data (with respect to unfiltered DNS data). Two wall-normal distances are considered,  $x_2 = 0.2\delta$  and  $x_2 = 0.75\delta$ . The error scales as  $\mathcal{E}_s \sim \Delta^{4/3}$ , consistent with estimations in Section 6.1, and are insensitive to variations in the Reynolds number  $\mathcal{E}_s \sim Re_\tau^0$ . When the error is expressed as a function of  $\Delta/\delta$ ,  $\mathcal{E}_s$  increases for decreasing wall-normal distances due to the smaller eddy size relative to  $\delta$ . Conversely, the errors collapse at different  $x_2$  locations when  $\Delta$  is normalized by  $L_s$ , as shown for the mean profile and turbulence intensities in previous sections. In summary, we conclude that the errors in the kinetic energy spectra follow

$$\mathcal{E}_s \sim \left(\frac{\Delta}{L_s}\right)^{4/3} Re_\tau^0. \quad (53)$$

## 7. Conclusions

Large-eddy simulation has emerged as a fundamental tool for both scientific research and industrial applications. However, the solutions provided by implicitly-filtered LES are grid-dependent, and multiple computations are required in order to attain meaningful conclusions. This brings the fundamental question of what is the expected LES error scaling as a function of Reynolds number and grid resolution, which has been the aim of the present investigation. In particular, we have focused on the outer layer of wall-bounded flows at moderately high Reynolds numbers with grid resolutions comparable to the boundary layer thickness, as it is the typical scenario in wall-modeled LES for external aerodynamics.

We have argued that LES of wall-bounded turbulence is challenging since the energy-containing eddies are constrained to reduce their characteristic size in order to accommodate the presence of the wall. Proper wall-resolved LES calculations demand nested grid refinements to capture these eddies, with a high computational overhead. To make the problem tractable, previous studies have quantified SGS errors in WRLES at relatively low Reynolds numbers and unrealistically fine grids. In those conditions, most of the errors reported in the literature are probably dominated by the near wall-region, where SGS models are known to be deficient, while the contribution of SGS models in the outer layer is negligible due to the fine grid resolution. For example, we have shown that at  $Re_\tau \approx 1000$  and 20 points per  $\delta$ , the mean velocity profile in the outer layer is well predicted by WMLES without any explicit SGS model. Given that SGS models are mainly responsible for the outer flow in WMLES, it is necessary to consistently isolate the errors in the bulk flow from those in the near-wall region. It is only in this manner that we can faithfully evaluate the behavior of SGS models.

To assess the performance of SGS models in the outer region independently of the effect of the wall, we have designed a numerical experiment, referred to as exact-wall-stress channel flows, where the integrated effect of the near-wall region on the outer flow is bypassed by supplying the exact mean stress at the wall. This numerical experiment retains the same physics as the traditional channel flow far from the wall, and hence is a suitable framework to test boundary layer flows. We have considered two SGS models, i.e., dynamic Smagorinsky model and minimum dissipation model, that are representative of eddy viscosity models with and without test filtering, respectively.

We have investigated the error scaling of the mean velocity profile, turbulence intensities, and kinetic energy spectra, with the grid resolution and Reynolds number. The error is of the form

$$\mathcal{E}_q \sim \left(\frac{\Delta}{L}\right)^{\alpha_q} Re_\tau^{\gamma_q}, \quad (54)$$

where  $\Delta$  is the characteristic grid size,  $L$  is length scale of the energy-containing eddies, and  $q$  denotes the quantity the error  $\mathcal{E}_q$  is referred to, i.e.  $q = m$  for the mean velocity profile,  $q = f$  for the turbulence intensities, and  $q = s$  for the kinetic energy spectra. Our results show that  $\Delta/L$  is an intricate function of the flow state and grid resolution, but it is well approximated by the  $L_2$ -norm of  $(\Delta_1, \Delta_2, \Delta_3)$  divided by  $\delta$  for quantities integrated over the outer layer, and by the shear length-scale,  $L_s$ , for local errors as a function of the wall-normal direction. The observation of  $L_s$  as the relevant physical length-scale to normalize  $\Delta$  is consistent with its ability to represent the size of the energy-containing eddies as discussed by Lozano-Durán and Bae [56]. For  $Re_\tau > 1000$ , the errors are independent of the viscous effects and  $\gamma_q \approx 0$ , as expected for WMLES. We have derived the theoretical values of  $\alpha_q$  and compared the results with the empirical estimations obtained by numerical simulations. To be consistent with the current available computational resources, we have only considered grid resolutions which are a fraction of the boundary layer thickness. In these cases, the corresponding LES filter cut-off lies either in the shear-dominated regime or in the inertial range, and always

far from the viscous Kolmogorov region. We have showed that the grid resolution needs to be sufficient to resolve at least some fraction of the shear-dominated eddies in order to obtain  $\alpha_q > 0$ . Overall, our theoretical predictions match the numerical estimations, and we detail below the results of Eq. (54) for the different flow statistics investigated.

Errors in the mean velocity profile follow  $\mathcal{E}_m \sim \epsilon\Delta/\delta$ , where  $\epsilon$  is a SGS-model dependent constant. The local errors increase with the proximity of the wall, and we have shown that the prediction at the  $n$ -th off-wall grid point does not improve with grid refinement until the grid resolution approaches the WRLES regime.

We have reasoned that the turbulence intensities in implicitly-filtered LES are akin to those from filtered Navier–Stokes, but the former are controlled by the necessity of dissipating the energy input at the rate consistent with the statistically steady state, while the latter are directly linked to the filtering operation. In terms of convergence, the turbulence intensities are more demanding than the mean velocity profile and their error scales as  $\mathcal{E}_f \sim (\Delta/\delta)^{\alpha_f}$  with  $\alpha_f \approx 0.4 - 0.8$ . Furthermore, in order to correctly capture the classic wall-normal logarithmic dependence of the streamwise and spanwise turbulence intensities, the grid resolution must be comparable to the sizes of the eddies in the inertial range.

Errors in the wall-parallel kinetic energy spectra follow  $\mathcal{E}_s \sim (\Delta/L_s)^{4/3}$ . We have pointed out that SGS models affect the distribution of energy via two mechanisms, namely, eddy-viscosity dissipation and wall-normal eddy-viscosity transport, but the former is ten times larger in magnitude than the latter. The energy spectra from DNS was also utilized to estimate the LES grid requirements to resolve 90% of the turbulent kinetic energy as a function of  $x_2$ , resulting in  $\Delta_1 \approx \Delta_3 \approx 0.075x_2$ . For example, if we wish to accurately resolved 90% of the turbulent kinetic energy at  $x_2 \approx 0.5\delta$ , then  $\Delta_1 = \Delta_3 \approx 0.04\delta$ . If we further assume an isotropic grid, the count yields  $\sim 25$  points per boundary layer thickness.

In light of the present results, future efforts should be devoted to enhancing the convergence rate of SGS models. This may be desired to accelerate the convergence of the turbulence intensities in those cases where their accurate prediction is of significant importance. Examples are noise signature prediction, or particle laden flows at certain Stokes numbers. Additionally, since our work relies on a wall model providing the exact mean stress at the wall, we have to emphasize the importance of developing and assessing the accuracy of wall models as a pacing item to achieve practical LES.

## Acknowledgments

This work was supported by NASA under the Transformative Aeronautics Concepts Program, grant no. NNX15AU93A. The authors would like to thank Prof. Parviz Moin, Dr. Sanjeeb T. Bose, Dr. Perry Johnson, and Dr. Maxime Bassenne for their insightful comments.

## Appendix A. Error in the mean velocity profile for Vreman model, finer grids, and WMLES

Cases with the Vreman model (VRM) are computed using the same numerical set-up described in Section 3.2 with a Vreman constant equal to 0.1,  $Re_\tau \approx 4200$ , and grid resolutions i1, i2 and i3. We use the same nomenclature as in Section 3.2. The error in the mean velocity profile is shown in Fig. A.16(a) and follows  $\mathcal{E}_m \sim \Delta/\delta$  with values comparable to those obtained for AMD.

To test the effect of further grid refinements, two additional cases are computed with isotropic grids equal to  $\Delta = 0.0125\delta$  (denoted by i5) and  $\Delta = 0.0063\delta$  (i6) for DSM at  $Re_\tau \approx 4200$ . In order to alleviate the computational cost, the streamwise and spanwise channel lengths are reduced to  $2\pi\delta$  and  $\pi\delta$ , respectively. The error in the mean velocity profile is plotted Fig. A.16(a) which shows that  $\mathcal{E}_m \sim \Delta/\delta$  is recovered below  $\Delta \approx 0.05\delta$ .

Finally, we also include results, where the EWS condition from Section 3.1 is replaced by an actual wall model, namely, the equilibrium wall model by Kawai and Larsson [47] (EQWM). Cases are computed at  $Re_\tau \approx 4200$  for DSM and grid resolutions i1, i2 and i3. The linear scaling observed for cases with EWS deteriorates slightly when the wall model is introduced, but remains close to  $\mathcal{E}_m \sim \Delta/\delta$  as shown in Fig. A.16(b).

## References

- [1] J. Slotnick, A. Khodadoust, J. Alonso, D. Darmofal, W. Gropp, E. Lurie, D. Mavriplis, CFD Vision 2030 Study: A Path to Revolutionary Computational Aerosciences, Tech. Rep. CR–2014-218178, NASA, 2014.
- [2] S. B. Pope, Ten questions concerning the large-eddy simulation of turbulent flows, New Journal of Physics 6 (2004) 35.



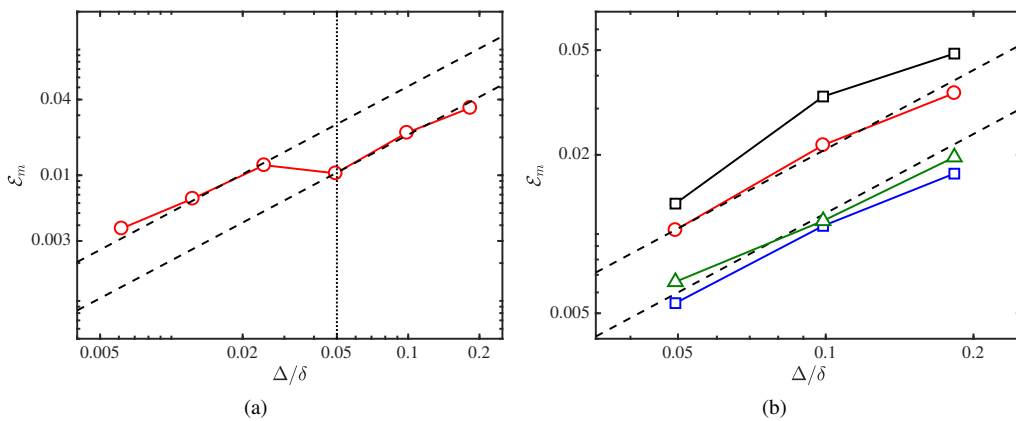


Fig. A.16: Error in the mean velocity profile as a function of the characteristic grid resolution  $\Delta = \sqrt{(\Delta_1^2 + \Delta_2^2 + \Delta_3^2)/3}$ . (a) Assessment of finer grid resolutions for DSM4200-EWS-i1,i2,i3,i4,i5,i6. (b) Assessment of Vreman model and equilibrium wall model by Kawai and Larsson [47]. Colors and symbols in (b) are (◦) for DSM4200-EWS-i1,i2,i3, (◻) for AMD4200-EWS-i1,i2,i3, (△) for VRM4200-EWS-i1,i2,i3, and (◻) for DSM4200-EQWM-i1,i2,i3. Dashed lines are  $\mathcal{E}_m \sim \Delta/\delta$ , and the dotted line is  $\Delta = 0.05\delta$ .

- [3] A. Leonard, Energy cascade in large-eddy simulations of turbulent fluid flows, in: F. Frenkiel, R. Munn (Eds.), *Turbulent Diffusion in Environmental Pollution*, volume 18 of *Advances in Geophysics*, Elsevier, 1975, pp. 237 – 248.
- [4] T. S. Lund, The use of explicit filters in large eddy simulation, *Comput. Math. App.* 46 (2003) 603–616.
- [5] D. Carati, G. S. Winckelmans, H. Jeanmart, On the modelling of the subgrid-scale and filtered-scale stress tensors in large-eddy simulation, *J. Fluid Mech.* 441 (2001) 119–138.
- [6] H. J. Bae, A. Lozano-Durán, Towards exact subgrid-scale models for explicitly filtered large-eddy simulation of wall-bounded flows, *Center for Turbulence Research - Annual Research Briefs (2017)* 207–214.
- [7] H. J. Bae, A. Lozano-Durán, DNS-aided explicitly filtered LES of channel flow, *Center for Turbulence Research - Annual Research Briefs (2018)* 197–207.
- [8] M. H. Silvis, F. X. Trias, M. Abkar, H. J. Bae, A. Lozano-Durán, R. Verstappen, Exploring nonlinear subgrid-scale models and new characteristic length scales for large-eddy simulation, *Center for Turbulence Research - Proceedings of the Summer Program (2016)* 265–274.
- [9] S. T. Bose, P. Moin, D. You, Grid-independent large-eddy simulation using explicit filtering, *Phys. Fluids* 22 (2010) 105103.
- [10] R. A. Clark, J. H. Ferziger, W. C. Reynolds, Evaluation of subgrid-scale models using an accurately simulated turbulent flow, *J. Fluid Mech.* 91 (1979) 1–16.
- [11] O. Métais, M. Lesieur, Spectral large-eddy simulation of isotropic and stably stratified turbulence, *Journal of Fluid Mechanics* 239 (1992) 157–194.
- [12] H. Kobayashi, Y. Shimomura, The performance of dynamic subgrid-scale models in the large eddy simulation of rotating homogeneous turbulence, *Phys. Fluids* 13 (2001) 2350–2360.
- [13] B. Vreman, B. Geurts, H. Kuerten, Large-eddy simulation of the temporal mixing layer using the clark model, *Theoretical and Computational Fluid Dynamics* 8 (1996) 309–324.
- [14] B. Vreman, B. Geurts, H. Kuerten, Large-eddy simulation of the turbulent mixing layer, *Journal of Fluid Mechanics* 339 (1997) 357–390.
- [15] U. Piomelli, P. Moin, J. H. Ferziger, Model consistency in large eddy simulation of turbulent channel flows, *Phys. Fluids* 31 (1988) 1884–1891.
- [16] M. Germano, U. Piomelli, P. Moin, W. H. Cabot, A dynamic subgrid-scale eddy viscosity model, *Phys. Fluids A* 3 (1991) 1760.
- [17] D. Chung, B. McKeon, Large-eddy simulation of large-scale structures in long channel flow, *Journal of Fluid Mechanics* 661 (2010) 341–364.
- [18] J. Bonnet, R. Moser, W. Rodi, A selection of test cases for the validation of large eddy simulations of turbulent flows, *AGARD advisory report* 345 (1998) 1–35.
- [19] S. Ghosal, An analysis of numerical errors in large-eddy simulations of turbulence, *J. Comp. Phys.* 125 (1996) 187 – 206.
- [20] A. Kravchenko, P. Moin, On the effect of numerical errors in large eddy simulations of turbulent flows, *J. Comp. Phys.* 131 (1997) 310 – 322.
- [21] F. K. Chow, P. Moin, A further study of numerical errors in large-eddy simulations, *J. Comp. Phys.* 184 (2003) 366 – 380.
- [22] J. Meyers, B. J. Geurts, M. Baelmans, Database analysis of errors in large-eddy simulation, *Phys. Fluids* 15 (2003) 2740–2755.
- [23] J. Meyers, B. Geurts, P. Sagaut, A computational error-assessment of central finite-volume discretizations in large-eddy simulation using a smagorinsky model, *J. Comp. Phys.* 227 (2007) 156 – 173.
- [24] J. Meyers, Error-landscape assessment of large-eddy simulations: A review of the methodology, *Journal of Scientific Computing* 49 (2011) 65–77.
- [25] J. Meyers, P. Sagaut, Is plane-channel flow a friendly case for the testing of large-eddy simulation subgrid-scale models?, *Phys. Fluids* 19 (2007) 048105.
- [26] P. P. Sullivan, E. G. Patton, The effect of mesh resolution on convective boundary layer statistics and structures generated by large-eddy simulation, *Journal of the Atmospheric Sciences* 68 (2011) 2395–2415.

- [27] R. J. A. M. Stevens, M. Wilczek, C. Meneveau, Large-eddy simulation study of the logarithmic law for second- and higher-order moments in turbulent wall-bounded flow, *J. Fluid Mech.* 757 (2014) 888–907.
- [28] H. B. Toda, O. Cabrit, K. Truffin, G. Bruneaux, F. Nicoud, Assessment of subgrid-scale models with a large-eddy simulation-dedicated experimental database: The pulsatile impinging jet in turbulent cross-flow, *Phys. Fluids* 26 (2014) 075108.
- [29] O. Lehmkuhl, G. Park, P. Moin, LES of flow over the NASA Common Research Model with near-wall modeling, Center for Turbulence Research - Proceedings of the Summer Program (2016) 335–341.
- [30] B. J. Geurts, J. Fröhlich, A framework for predicting accuracy limitations in large-eddy simulation, *Phys. Fluids* 14 (2002) L41–L44.
- [31] M. Klein, An attempt to assess the quality of large eddy simulations in the context of implicit filtering, *Flow, Turbulence and Combustion* 75 (2005) 131–147.
- [32] M. Freitag, M. Klein, An improved method to assess the quality of large eddy simulations in the context of implicit filtering, *Journal of Turbulence* 7 (2006) N40.
- [33] I. Celik, M. Klein, J. Janicka, Assessment measures for engineering les applications, *Journal of Fluids Engineering* 131 (2009) 031102–031102–10.
- [34] G. Nastac, J. W. Labahn, L. Magri, M. Ihme, Lyapunov exponent as a metric for assessing the dynamic content and predictability of large-eddy simulations, *Phys. Rev. Fluids* 2 (2017) 094606.
- [35] U. Piomelli, E. Balaras, Wall-layer models for large-eddy simulations, *Annu. Rev. Fluid Mech.* 34 (2002) 349–374.
- [36] O. Flores, J. Jiménez, Effect of wall-boundary disturbances on turbulent channel flows, *J. Fluid Mech.* 566 (2006) 357–376.
- [37] J. Lee, M. Cho, H. Choi, Large eddy simulations of turbulent channel and boundary layer flows at high reynolds number with mean wall shear stress boundary condition, *Phys. Fluids* 25 (2013) 110808.
- [38] Y. Mizuno, J. Jiménez, Wall turbulence without walls, *J. Fluid Mech.* 723 (2013) 429–455.
- [39] D. Chung, J. P. Monty, A. Ooi, An idealised assessment of townsend's outer-layer similarity hypothesis for wall turbulence, *J. Fluid Mech.* 742 (2014).
- [40] D. R. Chapman, Computational aerodynamics development and outlook, *AIAA J.* 17 (1979) 1293–1313.
- [41] H. Choi, P. Moin, Grid-point requirements for large eddy simulation: Chapman's estimates revisited, *Phys. Fluids* 24 (2012) 011702.
- [42] J. Jiménez, Cascades in wall-bounded turbulence, *Annual Review of Fluid Mechanics* 44 (2012).
- [43] J. Larsson, S. Kawai, J. Bodart, I. Bermejo-Moreno, Large eddy simulation with modeled wall-stress: recent progress and future directions, *Mechanical Engineering Reviews* 3 (2016) 15–00418.
- [44] P. P. Sullivan, J. C. McWilliams, C.-H. Moeng, A grid nesting method for large-eddy simulation of planetary boundary-layer flows, *Boundary-Layer Meteorology* 80 (1996) 167–202.
- [45] A. G. Kravchenko, P. Moin, K. Shariff, B-spline method and zonal grids for simulations of complex turbulent flows, *J. Comp. Phys.* 151 (1999) 757 – 789.
- [46] J. Jiménez, R. D. Moser, Large-eddy simulations: Where are we and what can we expect?, *AIAA J.* 38 (2000) 605–612.
- [47] S. Kawai, J. Larsson, Wall-modeling in large eddy simulation: Length scales, grid resolution, and accuracy, *Phys. Fluids* 24 (2012) 015105.
- [48] S. Chen, Z. Xia, S. Pei, J. Wang, Y. Yang, Z. Xiao, Y. Shi, Reynolds-stress-constrained large-eddy simulation of wall-bounded turbulent flows, *J. Fluid Mech.* 703 (2012) 1–28.
- [49] A. Rouhi, U. Piomelli, B. J. Geurts, Dynamic subfilter-scale stress model for large-eddy simulations, *Phys. Rev. Fluids* 1 (2016) 044401.
- [50] A. Rasam, G. Brethouwer, P. Schlatter, Q. Li, A. V. Johansson, Effects of modelling, resolution and anisotropy of subgrid-scales on large eddy simulations of channel flow, *J. Turbul.* 12 (2011) 1–20.
- [51] S. B. Pope, *Turbulent Flows*, Cambridge University Press, 2000.
- [52] A. E. Perry, C. J. Abell, Asymptotic similarity of turbulence structures in smooth- and rough-walled pipes, *J. Fluid Mech.* 79 (1977) 785 – 799.
- [53] J. Jiménez, Turbulent flows over rough walls, *Ann. Rev. Fluid Mech.* 36 (2004) 173–196.
- [54] O. M. Bakken, P. Å. Krogstad, A. Ashrafian, H. I. Andersson, Reynolds number effects in the outer layer of the turbulent flow in a channel with rough walls, *Phys. Fluids* 17 (2005) 065101.
- [55] O. Flores, J. Jiménez, J. C. del Álamo, Vorticity organization in the outer layer of turbulent channels with disturbed walls, *J. Fluid Mech.* 591 (2007) 145–154.
- [56] A. Lozano-Durán, H. Bae, Characteristic scales of townsend's wall attached eddies, *J. Fluid Mech.* in press (2018).
- [57] D. Chung, J. P. Monty, N. Hutchins, Similarity and structure of wall turbulence with lateral wall shear stress variations, *J. Fluid Mech.* 847 (2018) 591–613.
- [58] P. Orlandi, *Fluid Flow Phenomena: A Numerical Toolkit*, number 1 in *Fluid Flow Phenomena: A Numerical Toolkit*, Springer, 2000.
- [59] J. Kim, P. Moin, Application of a fractional-step method to incompressible Navier-Stokes equations, *J. Comp. Phys.* 59 (1985) 308–323.
- [60] A. A. Wray, Minimal-storage time advancement schemes for spectral methods, Technical Report, NASA Ames Research Center, 1990.
- [61] A. Lozano-Durán, H. J. Bae, Turbulent channel with slip boundaries as a benchmark for subgrid-scale models in LES, Center for Turbulence Research - Annual Research Briefs (2016) 97–103.
- [62] H. J. Bae, A. Lozano-Durán, S. T. Bose, P. Moin, Turbulence intensities in large-eddy simulation of wall-bounded flows, *Phys. Rev. Fluids* 3 (2018) 014610.
- [63] A. Lozano-Durán, M. J. P. Hack, P. Moin, Modeling boundary-layer transition in direct and large-eddy simulations using parabolized stability equations, *Phys. Rev. Fluids* 3 (2018) 023901.
- [64] D. K. Lilly, A proposed modification of the Germano subgrid-scale closure method, *Phys. Fluids A* 4 (1992) 633–635.
- [65] W. Rozema, H. J. Bae, P. Moin, R. Verstappen, Minimum-dissipation models for large-eddy simulation, *Phys. Fluids* 27 (2015) 085107.
- [66] A. W. Vreman, An eddy-viscosity subgrid-scale model for turbulent shear flow: Algebraic theory and applications, *Phys. Fluids* 16 (2004) 3670–3681.
- [67] S. Hoyas, J. Jiménez, Scaling of the velocity fluctuations in turbulent channels up to  $Re_\tau=2003$ , *Phys. Fluids* 18 (2006) 011702.
- [68] A. Lozano-Durán, J. Jiménez, Effect of the computational domain on direct simulations of turbulent channels up to  $Re_\tau = 4200$ , *Phys. Fluids* 26 (2014) 011702.
- [69] Y. Yamamoto, Y. Tsuji, Numerical evidence of logarithmic regions in channel flow at  $Re_\tau = 8000$ , *Phys. Rev. Fluids* 3 (2018) 012602.
- [70] W. K. Yeo, K. W. Bedford, Closure-free turbulence modeling based upon a conjunctive higher order averaging procedure, *Computational*

Methods in Flow Analysis (1988) 844–851.

- [71] G. S. Winckelmans, A. A. Wray, O. V. Vasilyev, H. Jeanmart, Explicit-filtering large-eddy simulation using the tensor-diffusivity model supplemented by a dynamic smagorinsky term, *Phys. Fluids* 13 (2001) 1385–1403.
- [72] A. N. Kolmogorov, The Local Structure of Turbulence in Incompressible Viscous Fluid for Very Large Reynolds' Numbers, in: *Dokl. Akad. Nauk SSSR*, volume 30, 1941, pp. 301–305.
- [73] J. Deardorff, A numerical study of three-dimensional turbulent channel flow at large Reynolds numbers, *J. Fluid Mech.* 41 (1970) 453–480.
- [74] A. Scotti, C. Meneveau, D. K. Lilly, Generalized smagorinsky model for anisotropic grids, *Phys. Fluids* 5 (1993) 2306–2308.
- [75] P. R. Spalart, W. H. Jou, M. Strelets, S. R. Allmaras, et al., Comments on the feasibility of LES for wings, and on a hybrid RANS/LES approach, *Advances in DNS/LES 1* (1997) 4–8.
- [76] F. X. Trias, A. Gorobets, M. H. Silvis, R. W. C. P. Verstappen, A. Oliva, A new subgrid characteristic length for turbulence simulations on anisotropic grids, *Phys. Fluids* 29 (2017) 115109.
- [77] H. Tennekes, H. Tennekes, J. Lumley, *A First Course in Turbulence*, MIT Press, 1972.
- [78] Y. Mizuno, J. Jiménez, Mean velocity and length-scales in the overlap region of wall-bounded turbulent flows, *Phys. Fluids* 23 (2011) 085112.
- [79] J. Larsson, S. Kawai, J. Bodart, I. Bermejo-Moreno, Large eddy simulation with modeled wall-stress: recent progress and future directions, *Mech. Eng. Rev.* 3 (2016) 1–23.
- [80] A. A. Townsend, *The structure of turbulent shear flow*, Cambridge Univ Press, 1976.
- [81] I. Marusic, J. P. Monty, M. Hultmark, A. J. Smits, On the logarithmic region in wall turbulence, *J. Fluid Mech.* 716 (2013) R3.
- [82] M. Hultmark, M. Vallikivi, S. C. C. Bailey, A. J. Smits, Turbulent pipe flow at extreme reynolds numbers, *Phys. Rev. Lett.* 108 (2012) 094501.
- [83] J. Jiménez, S. Hoyas, Turbulent fluctuations above the buffer layer of wall-bounded flows, *J. Fluid Mech.* 611 (2008) 215–236.
- [84] J. A. Sillero, J. Jiménez, R. D. Moser, One-point statistics for turbulent wall-bounded flows at reynolds numbers up to  $\delta^+ \approx 2000$ , *Phys. Fluids* 25 (2013) 105102.
- [85] A. Lozano-Durán, J. Jiménez, Effect of the computational domain on direct simulations of turbulent channels up to  $Re_\tau = 4200$ , *Phys. Fluids* 26 (2014) 011702.
- [86] M. Lee, R. D. Moser, Direct numerical simulation of turbulent channel flow up to  $Re_\tau \approx 5200$ , *Journal of Fluid Mechanics* 774 (2015) 395–415.
- [87] R. H. Kraichnan, The structure of isotropic turbulence at very high reynolds numbers, *J. Fluid Mech.* 5 (1959) 497–543.
- [88] G. Winckelmans, H. Jeanmart, D. Carati, On the comparison of turbulence intensities from large-eddy simulation with those from experiment or direct numerical simulation, *Phys. Fluids* 14 (2002) 1809–1811.
- [89] Y. Mizuno, Spectra of energy transport in turbulent channel flows for moderate reynolds numbers, *J. Fluid Mech.* 805 (2016) 171–187.
- [90] J. C. Del Álamo, J. Jiménez, P. Zandonade, R. D. Moser, Scaling of the energy spectra of turbulent channels, *J. Fluid Mech.* 500 (2004) 135–144.
- [91] D. Chandran, R. Baidya, J. P. Monty, I. Marusic, Two-dimensional energy spectra in high-reynolds-number turbulent boundary layers, *J. Fluid Mech.* 826 (2017) R1.
- [92] I. Marusic, J. P. Monty, Attached eddy model of wall turbulence, *Annu. Rev. Fluid Mech.* 51 (2019) null.
- [93] C. M. Millikan, A critical discussion of turbulent flows in channels and circular tubes, in: *Proceedings of the Fifth International Congress for Applied Mathematics*, Harvard and MIT, 1938.
- [94] W. R. B. Morrison, R. E. Kronauer, Structural similarity for fully developed turbulence in smooth tubes, *J. Fluid Mech.* 39 (1969) 117–141.
- [95] A. E. Perry, C. J. Abell, Scaling laws for pipe-flow turbulence, *J. Fluid Mech.* 67 (1975) 257–271.
- [96] K. J. Bullock, R. E. Cooper, F. H. Abernathy, Structural similarity in radial correlations and spectra of longitudinal velocity fluctuations in pipe flow, *J. Fluid Mech.* 88 (1978) 585–608.
- [97] K. Kim, R. J. Adrian, Very large-scale motion in the outer layer, *Phys. Fluids* 11 (1999) 417–422.
- [98] M. Guala, S. E. Hommema, R. J. Adrian, Large-scale and very-large-scale motions in turbulent pipe flow, *J. Fluid Mech.* 554 (2006) 521–542.
- [99] S. C. C. Bailey, M. Hultmark, A. J. Smits, M. P. Schultz, Azimuthal structure of turbulence in high Reynolds number pipe flow, *J. Fluid Mech.* 615 (2008) 121–138.
- [100] C. D. Tomkins, R. J. Adrian, Spanwise structure and scale growth in turbulent boundary layers, *J. Fluid Mech.* 490 (2003) 37–74.
- [101] J. P. Monty, J. A. Stewart, R. C. Williams, M. S. Chong, Large-scale features in turbulent pipe and channel flows, *J. Fluid Mech.* 589 (2007) 147–156.
- [102] S. Hoyas, J. Jiménez, Reynolds number effects on the Reynolds-stress budgets in turbulent channels, *Phys. Fluids* 20 (2008) 101511.